

Utah State University

DigitalCommons@USU

All Graduate Theses and Dissertations

Graduate Studies

12-2017

Wireless Power Transfer Roadway Integration

Trevor Gardner
Utah State University

Follow this and additional works at: <https://digitalcommons.usu.edu/etd>



Part of the [Engineering Mechanics Commons](#), and the [Structural Engineering Commons](#)

Recommended Citation

Gardner, Trevor, "Wireless Power Transfer Roadway Integration" (2017). *All Graduate Theses and Dissertations*. 6866.

<https://digitalcommons.usu.edu/etd/6866>

This Thesis is brought to you for free and open access by the Graduate Studies at DigitalCommons@USU. It has been accepted for inclusion in All Graduate Theses and Dissertations by an authorized administrator of DigitalCommons@USU. For more information, please contact digitalcommons@usu.edu.



WIRELESS POWER TRANSFER ROADWAY INTEGRATION

By

Trevor Gardner

A thesis submitted in partial fulfillment
of the requirements for the degree

of

MASTER OF SCIENCE

in

Civil and Environmental Engineering
(Structural Engineering and Mechanics)

Approved:

Marvin W. Halling, Ph.D
Major Professor

Marc Maguire, Ph.D
Committee Member

Ziqi Song, Ph.D
Committee Member

Mark R. McLellan, Ph.D
Vice President for Research and
Dean of the School of Graduate Studies

UTAH STATE UNIVERSITY
Logan, Utah

2017

Copyright © Trevor Gardner 2017

All Rights Reserved

ABSTRACT

Wireless Power Transfer
Roadway Integration

By

Trevor George Gardner, Master of Science

Utah State University, 2017

Major Professor: Dr. Marvin W. Halling
Department: Civil and Environmental Engineering

Integrating wireless power transfer (WPT) systems into the infrastructure represents a major hurdle in the large-scale adoption of electric vehicles (EVs). It is proposed that inductive power transfer (IPT) technology be directly embedded into a pavement structure. The successful integration of IPT systems has several requirements. First, the embedment process cannot interfere with the electrical performance of the IPT system. Also, the presence of the IPT system in the pavement structure cannot negatively affect the roadway's lifespan.

A direct embedment method into roadway materials was tested. The electrical properties of the IPT systems were monitored during the embedment process. Modifications were made to the IPT systems to optimize the electrical performance of the embedded coil. These methods were applied to a full scale embedded IPT system. This system will be used at Utah State's Electric Vehicle Research (EVR) facility to dynamically charge EVs.

The structural performance of directly embedded IPT systems has been evaluated. The tensile stresses that cause pavement cracking have been simulated in the surface of the embedded IPT test samples. These samples have been tested under cyclic loading conditions to simulate the fatigue conditions found in roadways. The stresses and number of loading cycles at which these samples developed cracking was recorded and analyzed. The electrical properties of the IPT samples were also measured and analyzed as the pads were testing under these loading conditions.

(101 pages)

PUBLIC ABSTRACT

Wireless Power Transfer

Roadway Integration

By

Trevor George Gardner, Master of Science

Utah State University, 2017

Major Professor: Dr. Marvin W. Halling
Department: Civil and Environmental Engineering

Electric vehicles represent a major accomplishment in the energy and transportation industry. Unfortunately, they are restricted to a small travel range because of limited battery life. Successful integration of wireless power transfer (WPT) systems into the infrastructure would remove the range restrictions of EVs. To successfully integrate this technology, several requirements must be met. First, the embedment process cannot interfere with the electrical performance of the inductive power transfer (IPT) system. Second, the presence of the IPT system in the pavement structure cannot negatively affect the roadway's lifespan.

Several systems were directly embedded in roadway materials. The electrical properties of the systems were monitored during the embedment process. Then modifications were made to the IPT systems to optimize the embedment process. These modifications were then applied to a full scale IPT system which is being used to dynamically charge EVs.

To test the structural performance of the systems, tensile stresses were applied to the pads to simulate traffic loading conditions. These tensile stresses were applied under cyclic loading conditions to simulate fatigue conditions found in roadways. The number of cycles, and stress at failure was recorded and analyzed. The electrical properties of the IPT pads was also measured and analyzed during the fatigue loading conditions.

CONTENTS

	Page
ABSTRACT.....	iii
PUBLIC ABSTRACT	v
CONTENTS.....	vii
LIST OF TABLES.....	ix
LIST OF FIGURES	x
LIST OF EQUATIONS	xiii
CHAPTER	
1. INTRODUCTION	1
1.1 Research Question	1
2. LITERATURE REVIEW	3
2.1 First Pilot Study of Embedded Inductive Power Transfer.....	3
2.2 Coil Design and Integration.....	4
2.3 Surface Cracking in Pavements.....	9
3. DEVELOPING EMBEDDED WIRELESS TRANSFER PADS.....	11
3.1 Electric Vehicle and Roadway Research Facility.....	11
3.2 Inductive Power Transfer Components	14
3.3 Embedment Material Selection	18
3.4 Component Testing.....	20
3.5 First Embedded Pad.....	23
3.6 Electrical Problems Associated With Concrete Embedment	30
3.7 Latest Embedded IPT Coil Design and Areas for Future Research	37
4. TESTING PROCEDURES	41
4.1 Cracking Mechanisms in Pavements.....	41
4.2 Fatigue Analysis	45
4.3 Fatigue Testing Set-up and Equipment	49
4.4 Determining f_r	51
4.5 Determining S_{max}	55
5. TESTING RESULTS.....	61
5.1 Fatigue Testing First Pad.....	61
5.2 Fatigue Testing Second Pad	67
5.3 Fatigue Testing Third Pad	73
5.4 Other Cracking Results.....	79
5.5 Summary of Results.....	80

6. CONCLUSIONS.....	83
REFERENCES	85
APPENDICES	86
Appendix A: Calculating Moment of Inertial for Two Assumptions	87

LIST OF TABLES

Table	Page
3-1 Component testing results	22
3-2 First embedded coil concrete mix design	27
3-3 Inductance vs cure time	28
3-4 Resistance after concrete pour	28
3-5 Long-term inductance and resistance values	30
3-6 Electrical properties of two wire embedded IPT pad	32
3-7 Electrical property changes of IPT coil without aluminum plate	34
3-8 Electrical property changes of IPT coil with Spray coated Litz wire.....	35
3-9 Electrical property changes of IPT coil with heat-shrink coating	36
3-10 Electrical property changes of final IPT coil.....	39
4-1 Classes of fatigue load (Lee & Barr, 2002)	47
4-2 Concrete cylinder split-tension test results	52
4-3 Core sample split-tension test results	52
4-4 28-day break tests	53
4-5 Summary of assumptions.....	59
5-1 First sample: change in electrical properties with crack size	67
5-2 Second pad change in electrical properties with crack size.....	72
5-3 Third pad change in electrical properties with crack size	79
5-4 Tensile strength at cracking for each pad	82

LIST OF FIGURES

Figure	Page
3-1 Electric Vehicle and Roadway (EVR) Research Facility.....	12
3-2 EVR Test track and Power Panels.....	13
3-3 Cross-section of prefabricated concrete channels	13
3-4 (a) Typical layout of a circular power pad. (b) Typical fields.....	16
3-5 Circular IPT system.....	17
3-6 PATH roadway module and pickup inductor cross section	18
3-7 Composite roadway design.....	20
3-8 Embedded Litz wire segments.....	21
3-9 Break test set-up	22
3-10 Concrete sample after failure.....	23
3-11 First coil to be embedded in concrete.....	24
3-12 Cross-section of Litz wire spacing	25
3-13 Modular concrete pad design.....	26
3-14 Pouring first inductor pad.....	27
3-15 Installation of the first concrete embedded IPT coil.....	29
3-16 Litz wire with nylon sheathing	31
3-17 IPT coil with two different wires.....	32
3-18 Test 3 IPT coil without aluminum plate	34
3-19 Test 4 Spray coated Litz wire	35
3-20 Test 5 heat-shrink coated Litz wire	36
3-21 Final IPT embedment design.....	38

Figure	Page
3-22 Close up of final pad vertically offset wire spacing	38
4-1 Roadway stresses from wheel loads	42
4-2 Thermal loading stress: (a) negative gradient; (b) positive gradient	44
4-3 Concrete S-N plot	48
4-4 SMASH laboratory load frame	50
4-5 Four-point bending test set up	50
4-6 Four-point bending test loading diagram.....	51
4-7 Split tension test set up	54
4-8 Split tension test.....	54
4-9 No discontinuity assumption cross-section	55
4-10 Concrete IPT pad Isometric and cross-section views.....	56
4-11 De-bonded discontinuity assumption	57
5-1 First fatigue test set-up	62
5-2 Hysteresis of first fatigue test	63
5-3 Pre-cracked pad	64
5-4 First Stage (100 cycles)	64
5-5 Second Stage (15,000 cycles).....	65
5-6 Load was increased to 9,000 lbs. (approximately 20,000 cycles)	65
5-7 Cracks ½ inch (approximately 25,000 cycles)	65
5-8 (approximately 27,000 cycles)	66
5-9 First pad post failure.....	66

Figure	Page
5-10 Hysteresis of second fatigue test	68
5-11 Pre-cracked pad	69
5-12 Second Stage (approximately 10,000 cycles).....	69
5-13 Third Stage (approximately 30,000 cycles).....	70
5-14 Crack ¼ inch wide, load increased (32,000 cycles)	70
5-15 Crack 3/8 inch wide, (35,000 cycles)	70
5-16 Crack ¾ inch wide, (36,000 cycles)	71
5-17 Failure (approximately 40,000 cycles).....	71
5-18 Second pad post failure.....	72
5-19 Third fatigue test set-up.....	73
5-20 Hysteresis of third fatigue test.....	74
5-21 Pre-cracked pad	75
5-22 Cracking develops	75
5-23 Crack 1/8 inch wide.....	76
5-24 Crack ¼ inch wide	76
5-25 Crack ½ inch wide	77
5-26 Pad after failure	77
5-27 Third pad post failure	78
5-28 Other Sample tested with four-point bending test.....	80
5-29 Other sample after failure.....	80
5-30 S-N testing results.....	82

LIST OF EQUATIONS

Equations	Page
3-1.....	14
3-2.....	15
3-3.....	15
4-1a.....	48
4-1b.....	48
4-1c.....	48
4-2.....	52
4-3.....	53
4-4.....	57
4-5.....	58
4-6.....	58

CHAPTER 1

INTRODUCTION

Electric Vehicles (EVs) are becoming a very important part of a sustainable future. Currently, large scale adoption of EVs is limited by several key factors including battery life and range limitations. Recent advances in Inductive Power Transfer (IPT) technology have made in-motion EV charging very appealing. Application of this technology would allow short range EVs to travel extended distances that were previously thought impossible because of battery limitations. Although there are still many challenges to overcome, charging electric vehicles wirelessly while they are in-motion is becoming a real possibility. Creating a Wireless Power Transfer (WPT) infrastructure is a multidisciplinary research domain. Much of the work currently being done on WPT focuses on improving the design of the components necessary to have efficient power transfer. There is still much that needs to be learned.

This paper focuses on the civil engineering challenges associated with electric roadways, specifically the electrical performance and structural implications from directly embedding WPT systems into pavement structures.

1.1 Research Question

The primary question this research plans to answer is *“How can wireless power transfer technology be efficiently embedded into pavement systems?”* In order to make Wireless Power Transfer (WPT) on roadways a reality, research needs to prove that once the systems have been embedded in a roadway they can meet certain requirements. To be

considered a viable option for electric vehicle (EV) charging the WPT roadway cannot cause electrical performance losses associated with roadway embedment, and the presence of the WPT system cannot negatively affect the long-term durability of the roadway. These requirements can be broken down into several subsequent questions that need to be answered:

1. What embedment method will maintain the IPT coils electrical efficiency?
2. How will the embedded IPT system respond to the stresses subjected to a normal roadway?
3. How will the embedded IPT system effect the durability of a pavement structure?

CHAPTER 2

LITERATURE REVIEW

Successfully charging EVs in-motion requires current wireless power transfer technology to be integrated into the infrastructure. Much research has been done to increase the efficiency of wireless power transfer; however, the methods associated with embedding these units in roadways is lacking. Before WPT can be implemented on a large scale, research and development must be done on the infrastructure supporting the WPT systems. It is important that the roadway structure provide a durable housing for the power transfer coil, and that the efficiency of the coil is not effected by the embedment methods or materials used. This chapter presents problems associated with previous embedment techniques used in other pilot studies, the most up to date design of WPT systems to be embedded in the roadway, and structural considerations for successful integration into the infrastructure.

2.1 First Pilot Study of Embedded Inductive Power Transfer

*Roadway Powered Electric Vehicle Project Track
Construction and Testing Program Phase 3D
(California Partners for Advanced Transit and Highways, 1994)*

This report details the construction and testing of a Roadway Powered Electric Vehicle proof-of-concept system constructed by the California program for advanced transit and highways (PATH). This project, which took place during the 1980's and early 1990's, is one of the first attempts at a roadway embedded power transfer system. This project required roadway modules, cores and conductors to be installed in long loops along

the roadway in order to generate an inductive magnetic field. Although the type of Inductive Coupling System (ICS) used in this pilot project is very different from recent power transfer systems, much can be learned from the embedment techniques used.

The roadway modules used in this pilot study housed the other WPT components. These modules were long channel shaped structures made from a mixture of epoxy and sand. The roadway modules were placed in a trench cut into the roadway and then grouted in place. The roadway cores, which were made of laminated steel, sat inside the channel of the roadway module. The aluminum conductive elements then sat inside the steel core and were potted with a sand polyester mixture. After installation, the entire configuration was overlaid with a thin layer of asphalt.

Along with being very complicated and expensive, this design caused serious mechanical failures almost immediately after construction. Problems arose when several voids formed in the sand/polyester mixture used to pot the conductors. Overall failure occurred during thermal loading when differences in the thermal expansion coefficients between the aluminum conductors and other parts of the roadway caused the power transfer cables to buckle. This report establishes how important roadway embedment techniques are to the overall success of a WPT system.

2.2 Coil Design and Integration

Inductive Power Transfer
(Covic & Boys, 2013)

This article reviews some of the latest developments in dynamic wireless power transfer systems. Although there are several types of WPT systems, only inductive power

transfer IPT systems are discussed. The authors define the electrical components necessary for an IPT system, methods to increase the efficiency, and engineering challenges that remain with implementing these systems into future roadways.

IPT systems transfer power wirelessly between a stationary primary coil and a pickup device usually installed under a vehicle's chassis. The mechanism of IPT uses principles from Ampere's and Faraday's laws. Ampere's law states that a magnetic field is created by an electric current. Faraday's law states that any change in the magnetic environment of a coil of wire will cause a voltage to be induced in the coil. When a voltage from a power source is induced in the primary coil a magnetic flux is created. The pickup coil (or secondary coil) will then capture this magnetic flux and change it into a current to be used by the electric vehicle.

Based on recent developments, the essential elements of a power supply and primary coil are:

1. *A utility to very low frequency (VLF) 3.0-30 kHz, or low frequency (LF) 30-300kHz power supply for energizing a track.*
2. *The track (coil) itself with its frequency compensation and magnetics construction methodology.*
3. *A pickup system for taking power magnetically from the track.*
4. *A controller for controlling the power transfer process to a dc output voltage.*

Among the engineering challenges to be overcome is the cost and development of embedding these IPT pads into the infrastructure. The fragile magnetic material (ferrite)

must be integrated into a concrete roadway to give a long service life electrically in a very hostile environment.

Electrification of roads: Opportunities and Challenges (Chen & Kringos, 2015)

This article explores potential materials, construction methods and maintenance of what it refers to as the electrification of roads or eRoads. The authors hope to draw awareness to the need for more interdisciplinary collaboration by pointing out unsolved issues in roadway integration. Specifically, this collaboration requires civil engineering disciplines to ensure eRoad's functionality for an extended service life. Cost will be a big factor in successful integration, the most economic approach will use roadway materials and construction methods that are similar to what is traditionally used in the transportation industry.

The two main materials used in roadway construction are asphalt and concrete. Asphalt is relatively cheap, easy to install and provides a comfortable surface to drive on. Concrete is stronger, more durable and needs fewer repairs. This paper assumes that the entire IPT system will be integrated into a pavement structure. Along with directly embedding the system into a roadway, a thin overlay of either concrete or asphalt could be useful. The authors cite several benefits for entirely embedding the IPT system into the roadway with an additional overlay:

1. *The (IPT) facilities can be protected against accidental or environmental loading damage, and also water ingress corrosion.*

2. *An overlay may act as a stress relief layer to improve structural integration and benefit the eRoad's long term performance*
3. *The maintenance and rehabilitation actions will be confined to only the overlay, which can be very cost-effective.*
4. *The safety issues relating to high voltage IPT systems can be avoided.*

The components that will need to be embedded are the primary coil, ferrite cores, backing plate and other sensors necessary for IPT. It is very important that the performance of the individual components is not affected by the roadway integration. The roadway structure must protect the fragile IPT facilities from a very hostile environment. If the IPT system is damaged during its service lifetime it will be prevented from functioning properly. The IPT system also cannot effect the structural integrity of the roadway. The long term performance of the eRoad will be a critical factor in maximizing the economic, social and environmental benefits of the entire system.

This article indicates that there are generally two options to embedding the charging facilitates inside the pavement surface: *(i) The IPT facilities are fixed in excavated pavement as a skeleton structure, which is then sealed and protected by extra road materials; (ii) The IPT facilities can be molded in prefabricated modules and then embedded into the pavement as an entity.* The goal of either method should be to prevent premature damages in the early service life and optimize the cost-effective long term maintenance.

Most premature pavement failures occur from the following mechanisms: repeated loading from traffic, climate-induced thermal contraction and expansion inside the

pavement, freezing and frost heave during the winter and moisture flow during thawing in spring. The embedded inductors will be structural discontinuities in the pavement, and therefore the pavement itself will be extremely susceptible to these types of failures. eRoads also will have a high risk of de-bonding failures around the discontinuous interfaces of the embedded IPT systems. Any failures of either the pavement structure or the electrical performance of the IPT systems could render the entire eRoad useless.

Regular maintenance will be especially important to prevent premature failures in the eRoad. Traditional road resurfacing protects against surface cracking, oxidation, and raveling. Surface cracking in an eRoad is a special concern because of water ingression into the sensitive electrical components. Resurfacing could be performed every few years to maintain the robustness and cost-effectiveness of the roadway pavement as a whole.

*A Novel Wireless Power Transfer
for IN-Motion EV/PHEV Charging
(Onar et al., 2013)*

This paper summarizes some of the recent research performed at Oak Ridge National Laboratory (ORNL). ORNL has investigated wireless power transfer since 2006. The Team at ORNL has successfully developed a coupling coil design; which has led to fabrication and experimental validation. The ORNL coil design relies on Litz cable coils over a soft ferrite structure housed in a non-magnetic case. Along with dynamically testing the WPT coils with an in-motion vehicle, ORNL has investigated insertion losses due to roadway surfacing materials.

The authors point out that it is likely that the primary coils will be embedded in either concrete or asphalt surfaces. To simulate the coil's insertion into a roadway surface,

ONRL obtained an aged slab of concrete approximately 4.33 inches thick to entirely cover the primary coil. The presence of the concrete adds an additional source of power loss to the system. Experiments showed a loss of 6.26W with only an air gap between the primary and secondary coil. When the concrete was placed between the primary and secondary coil there was an additional loss of 3.93W.

The losses due to the presence of materials between the primary and secondary coil are closely related to the material's relative permittivity and dielectric properties. The little research that has been done into these losses indicates that the electromagnetic loss can be as important as other resistive and ferrite core losses. It is possible that the design of the coils may need to be modified to minimize the electromagnetic losses from roadway embedment. The system's overall loss of efficiency due to being entirely embedded in a roadway material still needs to be explored.

2.3 Surface Cracking in Pavements

Analysis of periodic cracks in surface layer of pavement structures (Xu et al., 2010)

This article presents a study of the formation mechanism of periodic cracks in the surface layer of pavement structures. Although there are several different types of pavement crack patterns, these cracks usually occur in the bending zone of the pavement. Longitudinal cracks are the main type of cracking because of the location and direction of tensile stress that forms due to the wheel loads from traffic.

The authors numerically model several pavement structures in a software package in order to determine the mechanisms of crack initiation and growth. To simplify the

numerical model, a four-point bending beam model is established as the boundary conditions. The model has several layers, each layer is assigned a tensile strength and elastic modulus. The model is loaded to simulate wheel loadings from traffic conditions. This loading pattern places a tensile stress in the surface layer of the pavement structure between the two wheel loads.

Results indicate that the cracking process can be divided up into 3 stages. In the first stage two cracks initiate near the support points of the top surface when the tensile stress reaches its tensile strength. In the next stage more cracks appear in the bending zone between the two initial cracks. In the final stage no more new cracks form and the existing cracks become more open. It was found that the crack spacing was related to the tensile strength of the surface layer.

The Authors conclude, “*studies indicate that surface layer thickness has significant influence on the crack spacing while the effect of thickness of the base layer on the crack spacing is slight. The crack spacing increases linearly with increasing thickness of surface layer. Both the tensile strength and elastic modulus of the surface layer have significant influence on the crack spacing as well as the elastic modulus of base layer.*”

CHAPTER 3

DEVELOPING EMBEDDED WIRELESS TRANSFER PADS

Section 3 focuses on the research, development and testing process for embedding an efficient wireless power transfer system into a roadway structure. The chapter begins by discussing the research facilities used for testing and evaluating the embedded IPT coil. Then, a series of component testing is reviewed. The chapter gives special focus to the initial full scale embedded IPT system along with the electrical problems that arose from directly embedding the coils. Next, the latest embedment design is reviewed. The chapter ends by discussing areas of embedded IPT technology requiring further research. Inductive pavements are very new technology, and the research and testing associated with this technology is still in the beginning stages.

3.1 Electric Vehicle and Roadway Research Facility

The Electric Vehicle and Roadway (EVR) Research Facility is near the main campus of Utah State University in Logan. The EVR, and other facilities at USU researching EV adoption, are part of the Center for Sustainable Electrified Transportation (SELECT). The SELECT team is made up of a variety of different engineering disciplines across multiple campuses including Civil Engineering expertise from Utah State University and Purdue University, and Electrical and Mechanical Engineering expertise from Utah State University, Purdue University, Colorado University-Boulder, University of Colorado Colorado Springs and Olin College of Engineering.

The EVR facility was specifically designed to develop, test and showcase the

technology related to inductive pavements. Researchers at the EVR hope to overcome barriers associated with dynamic in-motion charging of EVs. One of the biggest challenges researchers face is integrating inductive technology into the infrastructure. The EVR facility is specifically designed to address this and other engineering challenges. The facility includes a systems integration building surrounded by a quarter-mile oval test track as shown in Figure 3-1. Figure 3-2 on the following page shows the test track with Power Panels.

The test track, that both surrounds and goes through the EVR facility, contains several segments of prefabricated cavities. These concrete channels are meant to house embedded modular IPT systems. Power panels are distributed along these segments of track to electrify and evaluate the prefabricated pavements containing the IPT coils. These sections of track, which are approximately 100 feet long, will allow for multiple embedded coils be placed in line with one another to dynamically charge electric vehicles.

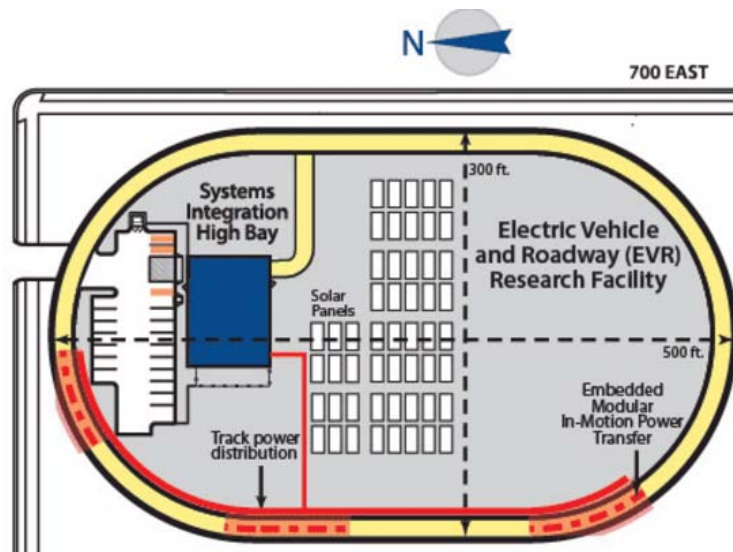


Figure 3-1 Electric Vehicle and Roadway (EVR) Research Facility

The exact size and geometry of embedded IPT systems are currently being developed. The prefabricated channels will give researchers the flexibility to test a variety of different embedded coil designs. The cross-section geometry of the channel is shown below in Figure 3-3.



Figure 3-2 EVR Test track and Power Panels

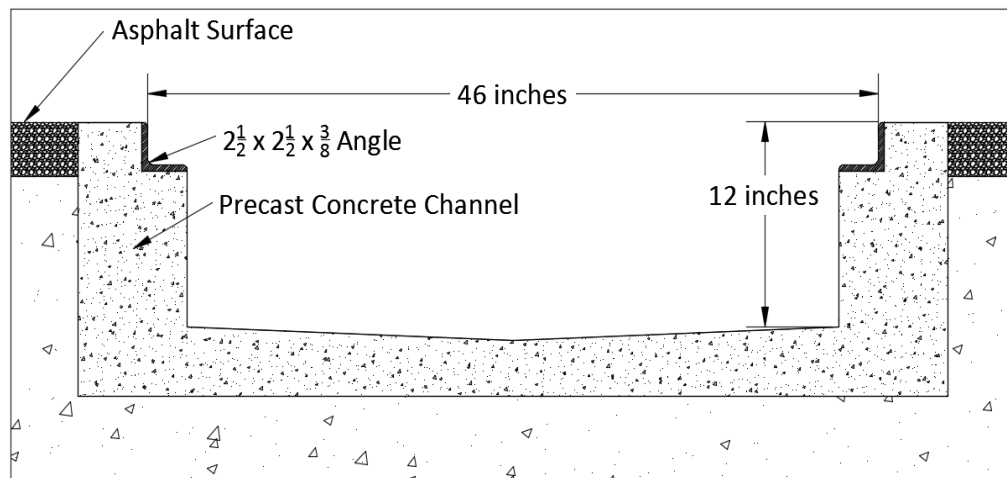


Figure 3-3 Cross-section of prefabricated concrete channels

Another unknown is the spacing needed between the various IPT pads and required vehicle sensors. These channels, and the supporting electrical infrastructure, will allow for the IPT pads and sensors to be adjusted as different spacing lengths are tested. Researchers expect to move from a modular design to a permanent embedded solution when sufficient testing has been completed.

3.2 Inductive Power Transfer Components

The components necessary for an embedded IPT system include Litz wire, ferrite, an aluminum backing plate and a skeletal structure to hold each of the components in place. These components are found to form a very efficient electromagnetic field when arranged in a circular pattern. Although more research and development is needed to optimize embedded IPT systems, attempts to embed these systems into the infrastructure will use the latest IPT coil technology. This section will begin by describing some of the latest methods and equations used to measure and optimize IPT system's effectiveness.

In *Inductive Power Transfer*, Covic & Boys (2013) point out that the efficiency of an IPT system is primarily determined from two parameters: the open circuit voltage induced in the pickup coil at frequency (ω) due to the primary track current (I_1) $V_{oc}=j\omega MI_1$, and its short circuit current $I_{sc}=MI_1/L_2$, which is the maximum current from V_{oc} that is limited by the impedance of the pickup coil inductance ωL_2 . These two parameters can be related by an equation given in (Covic & Boys, 2013). This equation is in terms of the volt-ampere (VA) of the pickup (secondary coil S_u).

$$S_u = V_{oc} I_{sc} = \omega I_1^2 \frac{M^2}{L_2} \quad \text{Equation 3-1}$$

The tuned quality factor Q is another important parameter to the overall performance of the system. Covic & Boys (2013) also state that: “*For a parallel-tuned regulator, this tuning enables the output voltage seen by the regulator to be increased in proportion to the circuit’s resonant Q , while for a series-tuned pickup, the output current is boosted by Q* ”. Adding this tuning factor to from (Covic & Boys, 2013) gives an equation that describes the output power in terms of frequency, inductance, impedance, current and Q .

$$P_{out} = S_u Q = \omega I_1^2 \frac{M^2}{L_2} Q \quad \text{Equation 3-2}$$

Covic & Boys (2013) also point out that along with optimizing the components necessary for the tuning of the system, the power transfer can be increased by increasing the frequency of the track’s current. The track’s (or coil’s) frequency is limited by the ratings of the semiconductor device used in the power supply, the Litz wire used in the track, and magnetic components (ferrite). As described in equation 3-2, the power output of an IPT system is quantified in terms of V_{oc} , I_{sc} and the operating Q of the receiver circuit. This equation can be rewritten in terms of VA and the input terminals of the primary pad ($V_{in}I_1$), the transformer coupling coefficient (κ), and the operating Q of the secondary coil.

$$P_{out} = P_{su} Q = V_{in} I_1 \kappa^2 Q \quad \text{Equation 3-3}$$

The coupling coefficient allows us to directly compare the magnetic properties of

different pad topologies. These properties can be easily determined by taking measurements with an inductor-capacitor-resistor (LCR) meter. An LCR meter will be used to determine the IPT systems efficiency before and after it is embedded in a roadway material.

Figure 3-4(a) (Covic & Boys, 2013) below shows a typical layout for a circular power pad, and Figure 3-4(b) (Covic & Boys, 2013) shows the magnetic flux fields generated by the primary pad. One of the most important aspects of an efficient IPT system is the Litz wire. The Litz wire used in IPT applications consists of many strands of copper wire woven together to form a single wire segment. These smaller strands of wire are electrically insulated from each other and designed to reduce the skin effect common in alternating current conductors. The Litz wire used in this type of IPT application usually has either 1600 or 2000 individual copper strands.

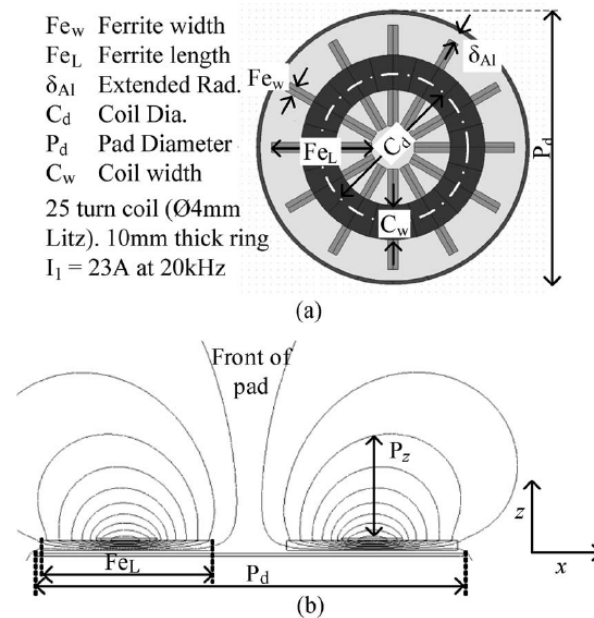


Figure 3-3(a) Typical layout of a circular power pad. (b) Typical fields.

Ferrite is a ceramic compound that consists of an iron oxide and other metals that when mixed together have ferrimagnetic properties. Ferrite is an important part of the IPT system because it helps shape the electromagnetic field generated by the current flowing through the Litz wire. Concerns have been raised over embedding the fragile ferrite material into a hostile roadway environment (Covic & Boys, 2013). Little is known about how the efficiency of the IPT pad will be effected if the ferrite bars develop cracks due to stresses from the roadway.

Covic & Boys (2013) state that the aluminum plate acts as a shielding from any flux leakages that may exist. The aluminum plate also provides a backing and adds robustness to the IPT system. The version of an IPT system that will be used for embedment purposes is shown in Figure 3-5. This circular IPT system contains the Litz wire, ferrite

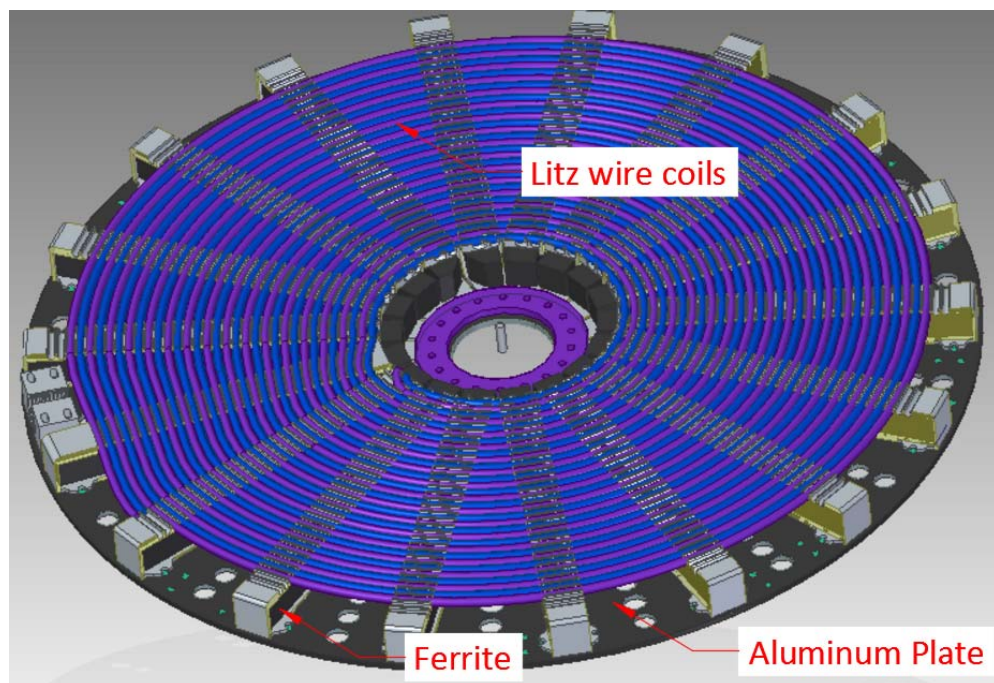


Figure 3-4 Circular IPT system

and an aluminum shielding plate. Because each of these components have very different properties, they will need to be considered separately concerning roadway integration.

3.3 Embedment Material Selection

Previous embedment attempts (California Partners for Advanced Transit and Highways (PATH), 1994) have failed because the methods of embedment were either too complicated or uneconomical. In PATH's pilot study, the method involved integrating roadway cores, which were made of laminated steel. These roadway cores sat inside the channel of the roadway module. The aluminum conductive elements then sat inside the steel core and were potted with a sand polyester mixture. After installation, the entire configuration was overlaid with a thin layer of asphalt, see Figure 3-6 below.

Unlike previous attempts, successful IPT integration will involve a minimal amount of different materials. An economic embedment solution would integrate IPT technology with materials that are already in use in roadway construction. Chen, et al (2015) discuss

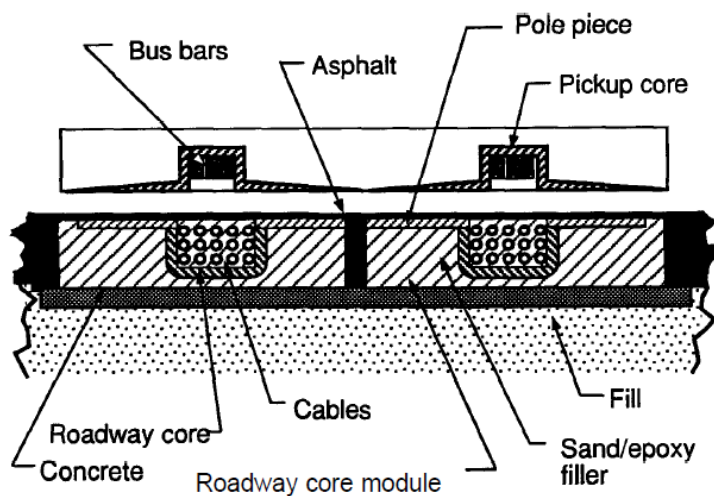


Figure 3-5 PATH roadway module and pickup inductor cross section

that the two main roadway embedment materials considered were asphalt (hot mix asphalt, HMA) or Portland Cement Concrete (PCC). Asphalt and concrete are relatively cost efficient and readily available in the transportation industry. Roadways are typically designed to have at least a 20-year lifespan. It is important that the materials selected for embedment support not only the roadway's lifespan, but an equally long lifespan for the embedded IPT system.

Concrete was initially chosen for an embedment material because it would provide a more durable structure to protect the fragile IPT components, such as the ferrimagnetic material (ferrite). Concrete is relatively cheap, easy to manufacture and can be modified based on the needs of its application. Once the IPT systems are embedded in concrete slabs they can easily be moved to different locations at the EVR facility. Asphalt is a relatively flexible material, and is subject to rutting and other structural deformations. Any structural deformations that may happen during the lifespan of an inductive roadway could have a very negative impact on the IPT system. Because both asphalt and concrete are subject to surface cracking, either material selected would require regular roadway maintenance.

Chen, et al (2015) also indicate that a possible embedment solution may be a composite roadway (i.e. a concrete structural PCC layer with a thin asphalt overlay as shown in Figure 3-7 on the next page). This design would utilize both the flexible properties of asphalt, and the structural properties of concrete. The authors believe the components of the IPT system would be protected by the concrete, and the asphalt would control cracking. While the work done in this chapter will support a composite roadway design, testing the effectiveness of an asphalt overlay will be beyond the scope of this research.

Roadway Cross Section:

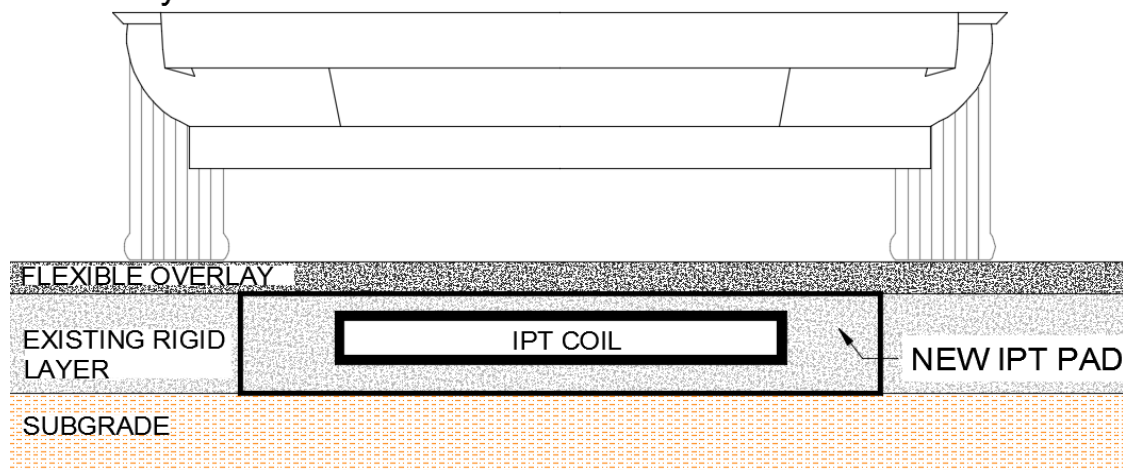


Figure 3-6 Composite roadway design

3.4 Component Testing

It was believed that the most economic approach was to directly embed the IPT system in concrete. Directly embedding the IPT system will also reduce the amount of discontinuities in the roadway, potentially allowing for a more durable pavement structure. The IPT components to be embedded include: Litz wire, ferrite, an aluminum shielding plate and the skeletal structure holding each of components in place during the embedment process. By directly embedding the IPT coils, each of the components will be directly exposed to the concrete.

There was an initial concern over the performance effects from directly embedding Litz wire in concrete. This concern led researchers to conduct a series of preliminary component tests on the Litz wire. This section reviews the component testing procedures and results when sections of Litz wire were embedded in concrete samples.

The goal of the component testing was not only to understand what effect directly embedding the Litz wire would have, but also what electrical properties may change as shear stress is induced in the concrete. Inductance and resistance are the critical electrical characteristics when considering IPT. By measuring the change in these two properties, researchers could understand what effect the concrete, and stress in the concrete, had on the wire. The inductance and resistance of the same Litz wire not embedded in a material was recorded to use as a control to measure the concrete's effect on the wire

Three rectangular concrete samples were made measuring 4 inches wide by 5 inches tall by 18 inches long. Three different types of concrete were used for the pseudo roadway material. One sample was a fast cure grout common in roadway construction, another was a non-shrink grout, and the final sample used a regular concrete mix.

The Litz wire was placed two inches from the top, and centered in each sample as shown in Figure 3-8. After the concrete samples cured, the resistance and inductance in the



Figure 3-7 Embedded Litz wire segments

wire was measured. In each of the samples, the concrete was found to have a negligible effect on the wire's electrical characteristics.

To understand how stress induced in the concrete would affect the performance of the Litz wire, a test was set up to break the samples in shear see Figure 3-9 below. The samples were gradually loaded until failure. The inductance and resistance of the wire were measured and recorded as the concrete approached failure. The results of the Litz wire concrete test is summarized in table 3-1. Figure 3-10 on the next page shows the samples after the shear failure.

Table 3-1 Component testing results

	Pre-Embedment	After Concrete pour	After Shear Failure
Roadway Grout	2.3 μH 0.016 Ω	2.29 μH 0.0159 Ω	2.31 μH 0.0155 Ω
Non-Shrink Grout	2.5 μH 0.018 Ω	2.45 μH 0.0182 Ω	2.45 μH 0.0160 Ω
Normal Concrete	5.9 μH 0.04 Ω	5.96 μH 0.0427 Ω	5.96 μH 0.0429 Ω



Figure 3-8 Break test set-up



Figure 3-9 Concrete sample after failure

Although the inductance and resistance values were measured throughout the shear test, the table above only reflects the initial and post-failure values. The other intermediate values are not recorded here because there seemed to be no observable change in either inductance or resistance as the concrete sample approached failure. The results from the component testing indicate that directly embedding the Litz wire in concrete and inducing a shear stress seems to have little effect on the electrical performance of the wire.

3.5 First Embedded Pad

After the series of Litz wire component testing was complete, the next phase was to directly embed a full scale IPT coil. This coil would allow researchers to monitor the material effects and power losses from directly embedding an IPT system into concrete. The coil, and surrounding concrete structure, would be designed to be placed in the

prefabricated concrete channels at the EVR. This design would allow researchers to dynamically test the efficiency of an embedded coil with an in-motion vehicle.

The first embedded coil, shown below in Figure 3-11, included: Litz wire, ferrite, an aluminum shielding plate, and the skeletal structure securing each of the components in place. The Litz wire used in the pad was #6 AGW wire. Based on previous research data, the target inductance of the pad would be $170\mu\text{H}$. To achieve the necessary inductance approximately 180 feet of Litz wire was used making a total of 27 individual coil wraps. The ferrite for the pad consisted of 18 ferrite spokes laid perpendicular to the wire. Each of the ferrite spokes were made up of three $\frac{3}{4}$ inch tall by 1 inch wide by 3.5 inches long ferrite segments. A 3-D printed plastic skeletal structure was made to hold the ferrite, coils of wire and the aluminum plate in place while the concrete was being poured.

Several structural modifications were made to the IPT coil design to allow for better concrete consolidation and structural integrity. One of these modifications required drilling

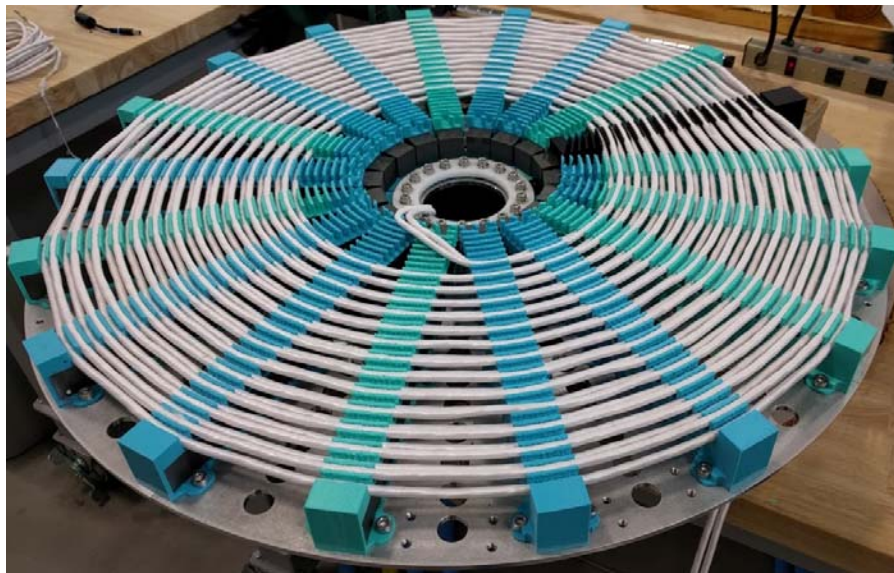


Figure 3-10 First coil to be embedded in concrete

many $\frac{3}{4}$ inch holes in the aluminum shielding plate to allow for better concrete permeation; these holes are shown in Figure 3-11. Another modification was to vertically offset the Litz wire coils from each other as shown below in Figure 3-12. It is also recommended that the spacing between wire coils should be approximately equal to the diameter of the wire itself. This wire spacing is also shown in Figure 3-12.

Structural reinforcement is common in PCC roadway applications. Most reinforcement is made from steel, which is a highly conductive material. There was an initial concern over how the presence of reinforcement in the pad would affect the electromagnetic flux of the IPT coil. Before the IPT coil was embedded, a matt of #4 rebar with 8-inch spacing was laid under the coil. It was determined that when the rebar was placed underneath the IPT coil there was a negligible effect on the coil's electrical performance. Based on these results, rebar reinforcement was used in the construction of the concrete structure for the first embedded coil.

FEM simulation and laboratory testing suggest (Vliet et al. 2005) that burying discontinuities in pavements at a depth of at least 2 inches or greater can minimize

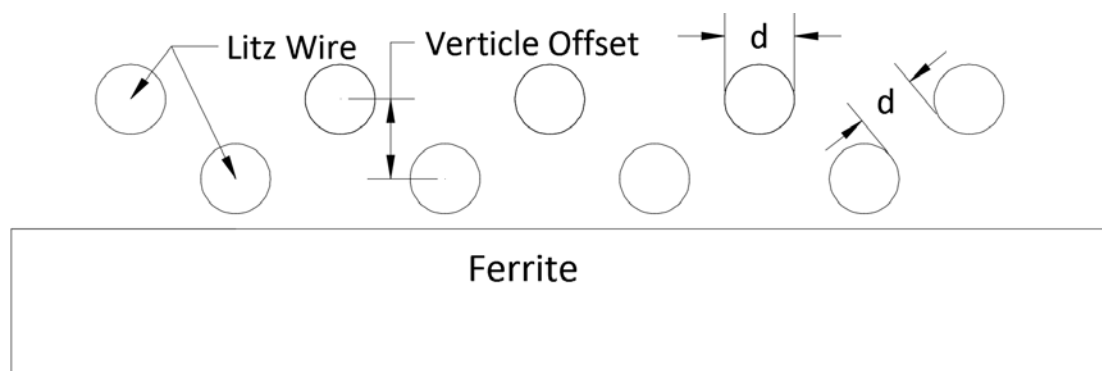


Figure 3-11 Cross-section of Litz wire spacing

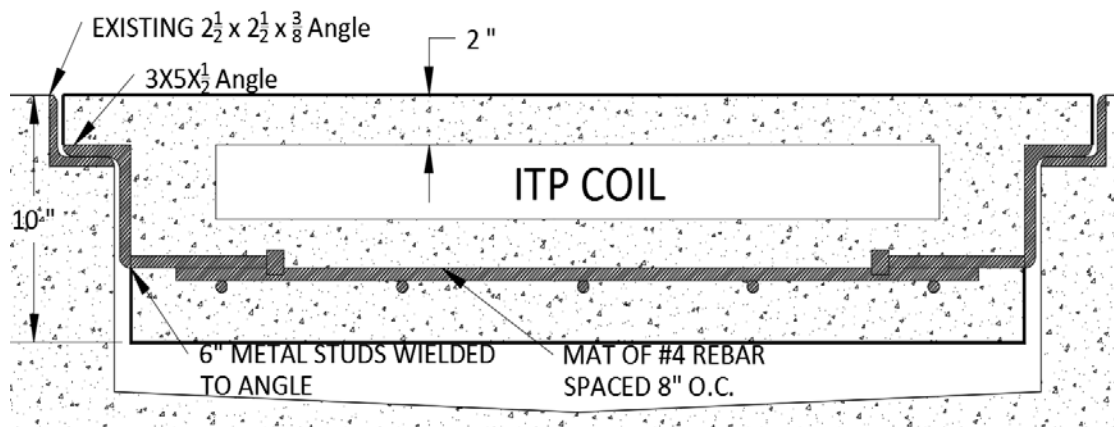


Figure 3-12 Modular concrete pad design

permanent deformation or shear failure of the roadway material around the discontinuities. Based on information from these sources, researchers embedded the top of the IPT coil 2 inches below the top surface of the concrete. A cross section of the concrete pad's dimensions, the IPT pad embedment depth and the rebar reinforcement is shown above in Figure 3-13.

The IPT system had very intricate parts, there was concern over how larger aggregate would consolidate around the components of the IPT coil. Researchers used a flowable concrete mix with only sand aggregate to maximize consolidation. A concrete vibrator was used to prevent voids, and ensure consolidation of the concrete around the IPT components as shown in Figure 3-14 on the next page. Table 3-2 shows the concrete mix design.

Before the embedment process began an inductor-capacitor-resistor (LCR) meter was used to measure the initial values of inductance and resistance. The meter was then used to monitor the inductance of the IPT pad during the pour. The inductance of the pad dropped from its initial value of $170.5\mu\text{H}$ to $3.15\mu\text{H}$ immediately after the coil was



Figure 3-13 Pouring first inductor pad

Table 3-2 First embedded coil concrete mix design

Material	Weight
Cement Powder	752 lb.
Flyash	188 lb.
Commercial Sand	2460 lb.
Entrapped Air	3.20 oz.
Low Range Water	37.60 oz.
Retarder	23.50 oz.
Non-Chloride Accelerator	376.00 oz.

covered with concrete. After the concrete pour, the LCR meter was used to periodically monitor the inductance level of the system throughout the next several days of the curing process. Table 3-3 below shows the change in inductance vs cure time following the concrete pour.

During the first concrete pour researchers were more concerned about the change in values of inductance rather than resistance. Because of this, the resistance data from the first concrete pour is minimal. Table 3-4 shows the recorded resistance data following the pour.

Table 3-3 Inductance vs cure time

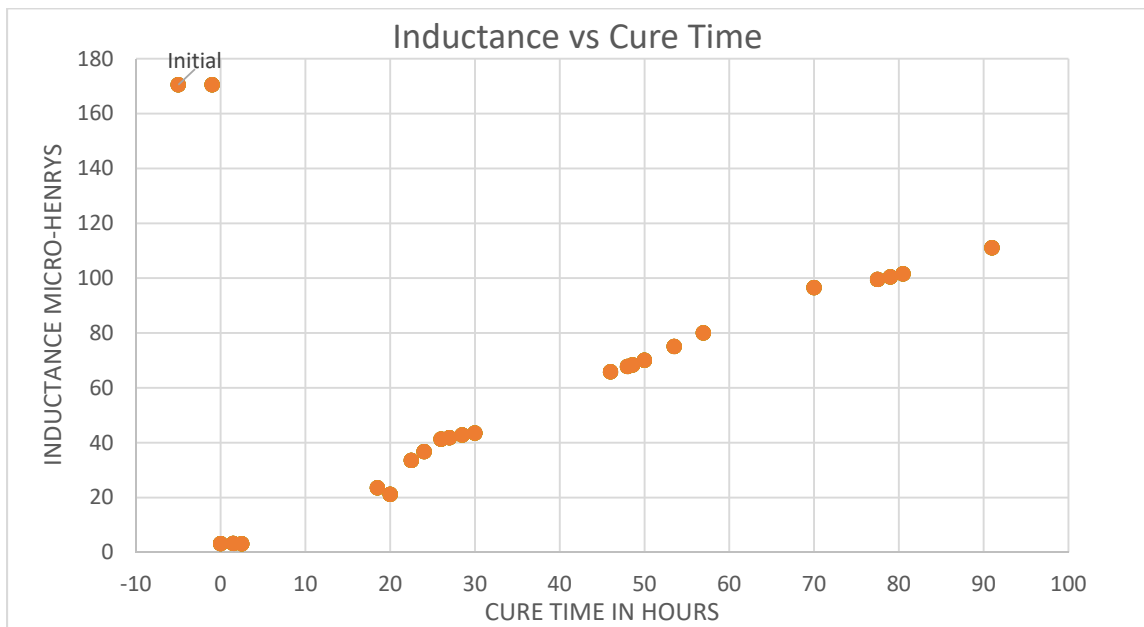


Table 3-4 Resistance after concrete pour

	Initial	1 hour	1 day
Resistance	.25 Ω	4.39 Ω	21.03 Ω

The concrete pad was moved to the track at the EVR 4 days after the pour. The IPT pad was inserted into the concrete channel inside the EVR building where it could be connected to a power source. At the time the embedded system was installed it was believed the electrical properties would return to their initial values when the concrete had fully cured. Figure 3-15 shows the concrete pad being installed at the EVR.

The resistance and inductance were monitored at the EVR following the concrete pad's installation. The IPT system would function properly only if the resistance and inductance returned to the initial values. Table 3-5 on the next page shows the long-term inductance and resistance values recorded at the EVR.



Figure 3-14 Installation of the first concrete embedded IPT coil

Table 3-5 Long-term inductance and resistance values

	Initial	28 days	60 days
Inductance	170.5 μ H	170.5 μ H	170.5 μ H
Resistance	.25 Ω	8 Ω	4.5 Ω

As shown in Table 3-5, the inductance of the embedded IPT system returns to the initial value of 170.5 μ H after the concrete has cured for 28 days. The resistance of the embedded system reaches a steady state value of 4.5 Ω s after the concrete has cured for 60 days. Because of the high resistance, this first embedded IPT pad will not be efficient and cannot be used to dynamically charge in-motion EVs.

3.6 Electrical Problems Associated With Concrete Embedment

Research and experimental studies indicate that an IPT coil needs to maintain an inductance level of approximately 170.5 μ H, and an ideal resistance level at or below .25 Ω . In the first concrete embedded IPT coil the inductance level returns to the initial value, but the resistance reaches a steady state value that is 18 times higher than the ideal resistance value. In order to find an IPT embedment solution researchers had to develop an IPT coil that would maintain these levels of inductance and resistance after the concrete was poured. This section discusses some of the methods used to keep the resistance and inductance levels of various IPT coils in the functioning range as the coil was embedded in concrete.

The Litz wire used in the first embedment attempt was wrapped in a thin nylon sheathing, see Figure 3-16 on the next page. Initially it was believed that the moisture from the wet concrete infiltrated the wire's sheathing, resulting in a negative effect on the wire's



Figure 3-15 Litz wire with nylon sheathing

performance. It was expected that by using version of Litz wire with a waterproof sheathing, these electrical issues could be avoided.

An IPT coil was set up with two types of Litz wire. One wire was the same nylon jacketed wire as used in the first embedment attempt. The other Litz wire was a black, plastic coated wire that was believed to be completely waterproof see Figure 3-17 on the next page. Everything else about the IPT coil was the same including the ferrite, the aluminum plate, rebar reinforcement and the skeletal structure holding the components in place (note: there were less ferrite spokes than used in the first embedment attempt).

The goal of this test was to replicate the results seen in the first embedment attempt with the white wire, and show that the black plastic coated wire was resistant to these electrical issues. Because this IPT pad was only made to test the electrical performance of the system, it was made using a smaller concrete form. The dimensions of the concrete form are 36 inches wide, 36 inches long, and 6 inches deep.

The same flowable concrete mix used in the first embedment attempt was used in this test. As soon as the concrete was poured the inductance in both wires dropped and the resistance began to rise. Table 3-6 below shows the initial electrical properties, as well as the changes in these properties after the pour.

Results from this test indicate that the plastic coated Litz wire undergoes almost the

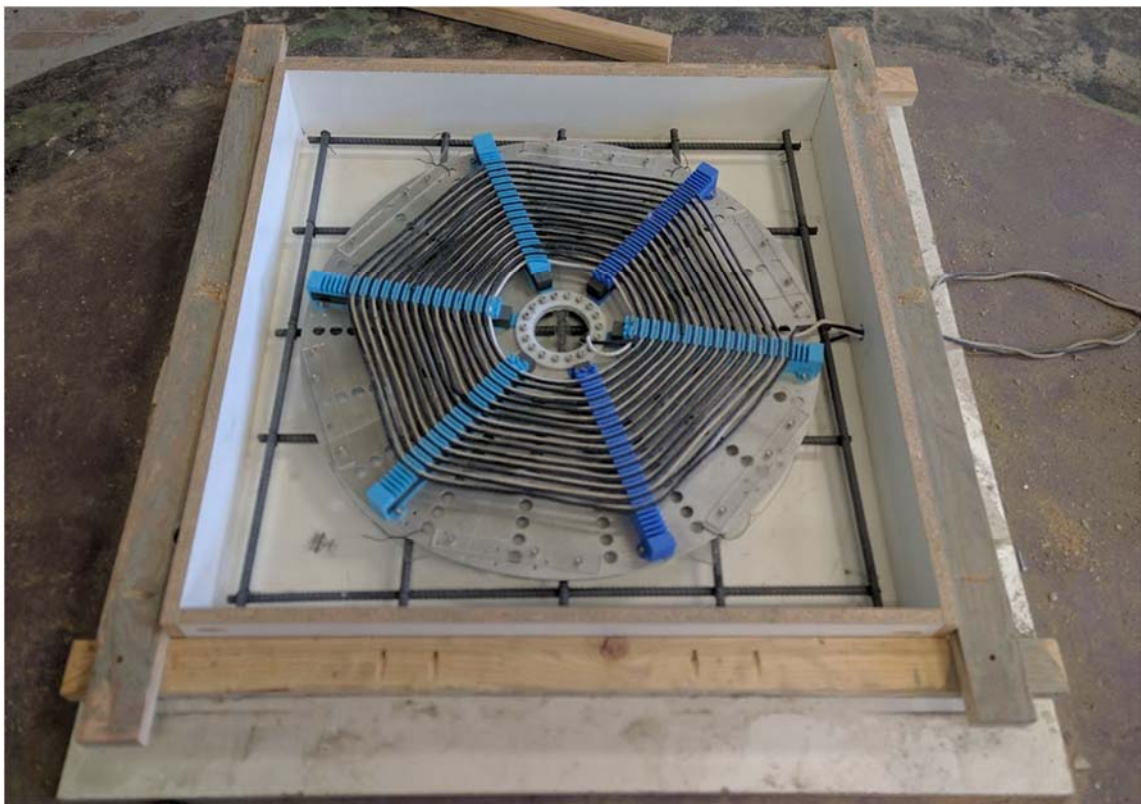


Figure 3-16 IPT coil with two different wires

Table 3-6 Electrical properties of two wire embedded IPT pad

	Initial Values	After Pour	8 Days	28 Days
Black Wire	111.85 μH 0.256 Ω	9.97 μH 3.58 Ω	117.73 μH 0.836 Ω	117.7 μH 0.94 Ω
White Wire	111.6 μH 0.257 Ω	10.55 μH 4.10 Ω	120.86 μH 0.933 Ω	119.03 μH 1.01 Ω

same electrical changes that are experienced by the nylon jacketed wire. Both wires experience less drastic changes than the first embedded pad. This could possibly have resulted from the shorter lengths of Litz used in this test. As in the previous test, the inductance in both wires seems to return to the initial amount. The ending resistance in the black wire is 3.7 times higher than the initial value, and the ending resistance in the white wire is 3.9 times higher than the initial value. Changing the Litz wire coating seemed to have little effect on maintaining the electrical properties of the pad.

Researchers then believed that the presence of the aluminum plate may have some effect on the electrical system when in concrete. The next test involved removing the aluminum plate from the embedded system. The aluminum plate was substituted with a circular sheet of $\frac{3}{4}$ inch plywood (see Figure 3-18 on the next page). This plywood was only meant to help hold the IPT system in place as the concrete was poured. For consistency, the white Litz wire with the nylon jacket was used for this test. The IPT coil for this test also contained ferrite and rebar reinforcement. When the test was performed, the same negative electrical trends were observed as in the previous tests. Table 3-7 on the next page summarizes the results.

Results indicate that the aluminum plate has little effect on the increase in resistance observed during the embedment process. The general trend observed in each test is the inductance will decrease immediately following the pour, then return to its initial value after the concrete has cured. The resistance will increase following the pour, then reach a steady state value that is anywhere from 3.7 to 18 times higher (depending on the size of the pad) than the initial value after the concrete has cured.



Figure 3-17 Test 3 IPT coil without aluminum plate

Table 3-7 Electrical property changes of IPT coil without aluminum plate

	Initial Values	After Pour	8 Days	28 Days
White Wire	110.75 μ H 0.0588 Ω	.29 μ H 8.65 Ω	111.1 μ H 0.60 Ω	111.7 μ H 0.488 Ω

Test 2 indicates that the plastic-coated wire experiences the same resistance increase when embedded in concrete. Although testing shows that just waterproofing the wire has little effect, it was believed that the thickness of coating over the wire may have some effect on the wire’s interaction with the concrete. The next test involved using a spray-on rubber coating over the same type of white, nylon jacketed Litz wire as used in previous tests. In this test, the IPT coil to be embedded only consisted of the coated Litz

wire; the aluminum plate, rebar reinforcement, and ferrite were omitted from the test (Figure 3-19 shows the coil to be embedded). Table 3-8 summarizes the results of the test.

The approximate thickness of the rubberized coating over the wire was 0.029 inches. In this test the inductance level never decreased like it was observed in previous tests. The Resistance level increased after the pour then reached a value that was 2.7 times higher than the initial value after 8 days of curing. These results seemed to indicate that the thickness of coating over the wire influences both the inductance and resistance of the system when it is embedded in concrete. It was difficult to get a consistent rubber thickness over the surface of the wire using the spray-on coating.

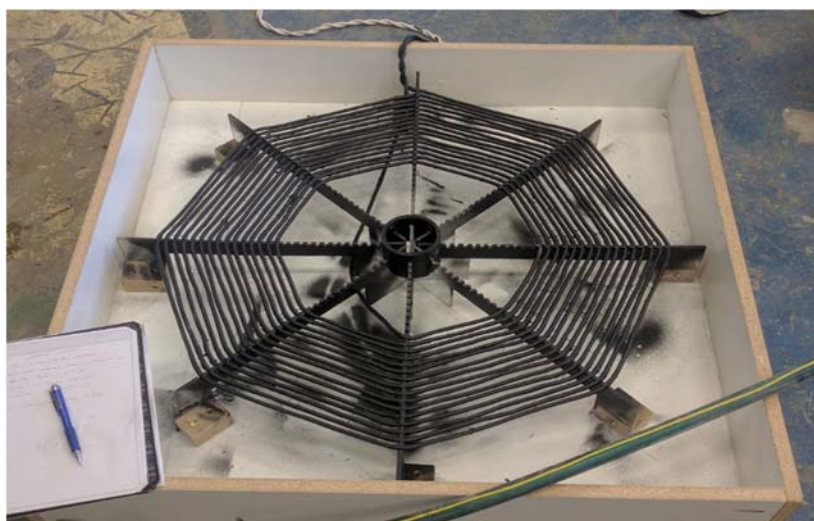


Figure 3-18 Test 4 Spray coated Litz wire

Table 3-8 Electrical property changes of IPT coil with Spray coated Litz wire

	Initial Values	After Pour	2 Days	8 Days
Spray Coated Wire	174.9 μH 0.15 Ω	179.7 μH 3.85 Ω	177.4 μH 0.59 Ω	177 μH 0.41 Ω

The next test implemented a type of rubberized heat-shrink coating over the same type of white, nylon jacketed Litz wire. Results from the previous test showed that a coating of at least 0.029 inches would benefit the embedded electrical performance of the IPT system. To achieve this coating thickness, two coats of heat-shrink were applied. This test included the ferrite bars, but the aluminum plate and rebar reinforcement were omitted from the test (see Figure 3-20 on the previous page). The results of the test are shown in Table 3-9 below. There was almost no change in the inductance and very little change in the resistance following the concrete pour.



Figure 3-19 Test 5 heat-shrink coated Litz wire

Table 3-9 Electrical property changes of IPT coil with heat-shrink coating

	Initial Values	After Pour	8 Days	28 Days
Heat-shrink coated wire	128.8 μH 0.0356 Ω	128.5 μH .0401 Ω	125.7 μH 0.0472 Ω	128.5 μH 0.0403 Ω

The factors involved in this series of testing included the type of Litz wire, the aluminum plate, and the thickness of the rubber coating around the wire. Researchers found that the thickness of coating around the Litz wire had the biggest influence on maintaining the electrical properties of the IPT system as it was embedded in concrete. The embedment methods developed in this series of testing are used in later embedded IPT coil designs.

3.7 Latest Embedded IPT Coil Design and Areas for Future Research

This section describes the latest embedded IPT coil design. The embedment methods developed in this chapter, and other structural considerations, were incorporated into the design to provide a long lasting IPT solution. IPT roadways are a very new technology, and the embedment solutions developed in this chapter are not complete. This section ends by discussing areas related to roadway embedded IPT technology that will require future research.

In the previous section researchers discovered that a coating thickness of at least .029 inches prevented some of the negative electrical property changes when the IPT coil is embedded in concrete. In the latest embedded coil, researchers used two coats of 0.015 inch thick heat-shrink coating around the Litz wire in the IPT system. The same wire spacing was used with the vertical offset as the first embedded pad (see Figure 3-21 and Figure 3-22 on the next page). The ferrite bars were included in the embedded IPT system. The aluminum plate used in several of the previous embedment methods presents a large discontinuity in the roadway surface. Considering the effect these discontinuities will have on the inductive roadway's lifespan, the aluminum plate was omitted from the embedded IPT coil design.



Figure 3-20 Final IPT embedment design



Figure 3-21 Close up of final pad vertically offset wire spacing

Table 3-10 Electrical property changes of final IPT coil

	Initial Values	After Pour	8 Days	21 Days
Final Pad	170.10 μ H 0.204 Ω	170.00 μ H 0.200 Ω	170.34 μ H 0.189 Ω	170.3 μ H 0.200 Ω

The initial inductance of the pad was 170.10 μ H and the resistance was 0.2036 Ω . The same methods of concrete consolidation were used in the final IPT pad pour. The initial inductance and resistance values, along with the change in the values during and after the pour, are recorded in Table 3-11 above. As the results from the table indicate, the changes in electrical properties during the final IPT pad pour are negligible. It is believed that the consistent electrical properties during the pour are the result of the coating around the Litz wire. After the concrete IPT pad had cured for 21 days it was installed in the track at the EVR facility. The performance of the embedded IPT system will continue to be evaluated as it is used to dynamically charge EV's.

Preliminary research and testing has shown that directly embedding an IPT charging system in a roadway is practical. Among the challenges associated with directly embedding the system is maintaining the same electrical characteristics of the IPT pad after it is embedded. Testing has shown these electrical characteristics are less subject to negative changes when the Litz wire has received at least a 0.029 inch rubber coating. Further testing and evaluation is needed to confirm the long-term performance of the embedded system as it is used in a practical application.

IPT systems are an evolving technology, possible changes may be made to the geometry of the coils, the ferrite components and other mechanical characteristics in order to improve their charging performance. It is very important that future roadway embedment

is considered as these changes are developed. The most efficient design will not only support the electrical performance of the IPT coil, but also the long term mechanical performance of the system and the roadway structure it is embedded in.

CHAPTER 4

TESTING PROCEDURES

This chapter begins by discussing some of the common reasons for pavement failures in roadways. Roadways are designed to withstand both traffic and environmental loading conditions. Common roadway failures are usually caused by one or a combination of these loading conditions. Future inductive pavements are expected to have the IPT system embedded near the surface of the pavement structure. It is important that the performance of the IPT system is not effected by the stress produced from the roadway's loading events. It is also important that the embedded IPT system does not reduce the roadway's normal lifespan. An efficient design will allow an inductive pavement structure to have the same lifespan as a typical roadway.

The goal of this chapter is to first understand the stresses that lead to cracking in typical roadways, and then use these stresses to test and measure the structural integrity of embedded IPT systems. Repeated tension loading events from traffic or the environment are the main cause of cracking and deterioration in pavement surfaces. This chapter identifies and discusses a simplified approach to simulate these types of loading conditions. These loading conditions can then be used to test the structural and mechanical properties of an embedded IPT system.

4.1 Cracking Mechanisms in Pavements

Cracking of the pavement surface of future inductive roadways could lead to a complete failure of the electrical system. Cracking will damage sensitive electrical

components and expose these components to contaminants like water, sodium chloride and other harmful substances. Cracks in roadways are due to tensile forces acting in the top surface of the pavement. These tensile forces can come from a variety of sources, but the two most common sources are wheel loads from traffic and temperature gradients. If Embedded IPT systems are to function properly throughout the entire lifespan of a roadway, they need to be designed with these roadway stresses in mind.

Wheel loading is the most common type of roadway loading. Most roadways will typically see several hundred thousand cycles of wheel loads during their service lifespan. The American Association of State Highway and Transportation Officials (AASHTO) specifies that a roadway must be designed to withstand a HS-20 truck wheel load (AASHTO 1993). This standard calls for a single axle load of 32 kips to be carried by 2 wheels, 16 kips to each wheel. Each wheel has a contact area of 200 square inches. It is important that future inductive roadways be designed to considering this standard.

Wheel loading causes a moment in the pavement structure, which produces both a compression and tension stress in the surface of the roadways (shown in Figure 4-1).

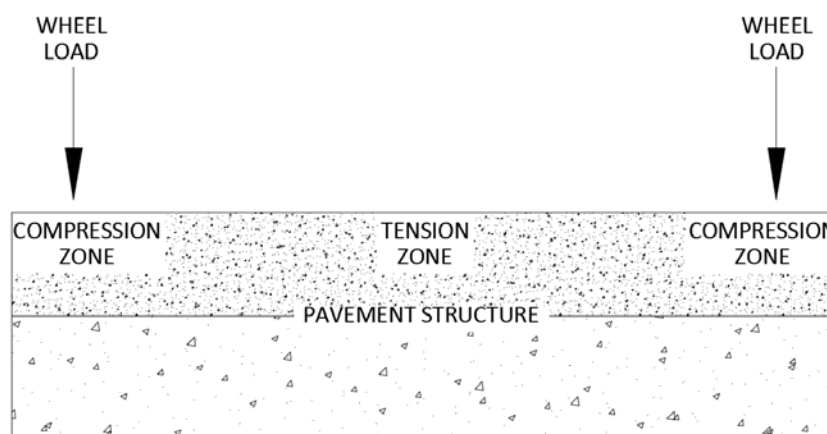


Figure 4-1 Roadway stresses from wheel loads

The figure shows how the two wheel loads can be simplified to represent two point loads on both sides of the pavement cross section. There are many patterns of pavement surface cracks, but most cracking happens in the bending zone (center) of the pavement structure. This common cracking location is a special concern for IPT integration because it will be directly over the embedded IPT system.

Temperature gradients are the other source of large tensile stresses found in the surface layer of pavement structures. Temperature gradients are defined as the change in temperature with displacement. Specifically, the change in temperature across the thickness of the roadway material will be considered. There are two types of temperature gradients found in roadways: positive and negative. The authors of (Dere, et al. 2006) state: *“The temperature gradient that causes the top slab surface to cool is termed a negative temperature gradient. Similarly, the temperature gradient that causes the top slab surface to warm is called a positive temperature gradient”*. Both loading conditions can have an adverse effect on the structural performance of the pavement. The loading conditions associated with temperature gradients will fluctuate with daily and seasonal temperature changes.

Because tensile forces are the main reason for surface cracking in pavement, this chapter will focus mainly on the effects from the negative temperature differential. A negative temperature differential is caused when external temperature conditions lower. The gradient resulting from this change in temperature creates a tensile force in the surface of the pavement structure. This tensile force causes the edges of the slab or roadway to curl

upward (see Figure 4-2(a) below). Also, because of the curled edges, the tensile stress is amplified with the addition of wheel loads.

Alternatively, a positive temperature gradient is created when external temperature conditions increase. This creates a temperature gradient that forces the top layer of the pavement into compression forcing the edges of the pavement down (see Figure 4-2(b) below). It has been shown in (Dere, et al. 2006) that both linear and nonlinear temperature profiles are found in roadways structures. Although the stresses can vary greatly based on the type of profile felt. An in-depth study of the effect of the different temperature profile types is beyond the scope of this research. The temperature gradient effects are very small in the sub-pavement layers, therefore only the top surface temperature gradient is considered.

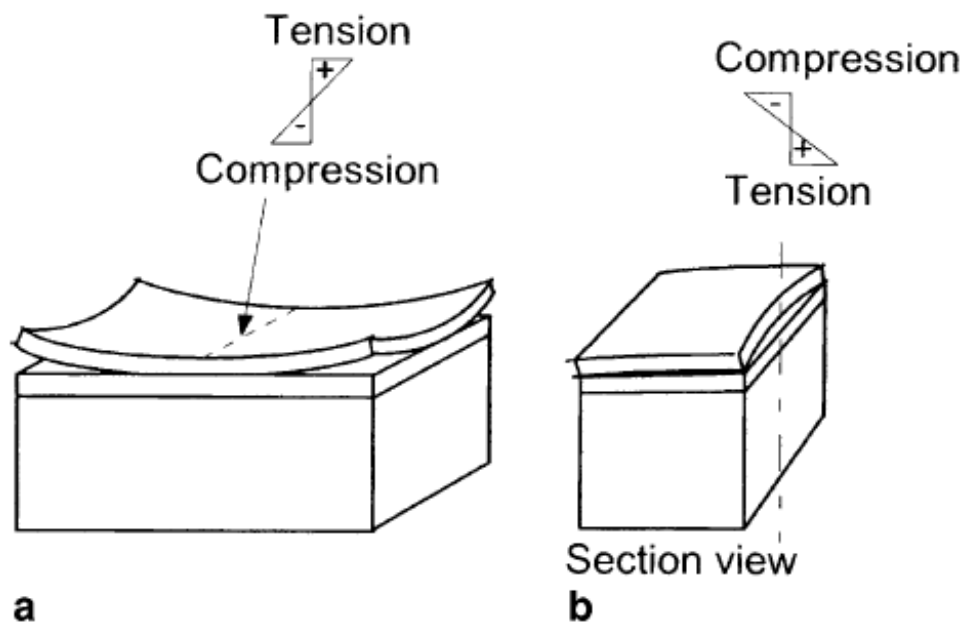


Figure 4-2 Thermal loading stress: (a) negative gradient; (b) positive gradient

For simplicity, the tensile stress from the wheel loads and the tensile stress from the negative thermal gradient will be considered as one loading event. (Dere, et al. 2006) used a FE model with medium-stiff clay base layer to model the stress distribution in a plain 9-inch-thick concrete pavement. The model showed a maximum tensile stress of approximately 310 psi (2131 kPa) when just the thermal loads were considered. When the AASHTO HS-20 truck wheel load was also present, the maximum tensile stress increased to approximately 392.6 psi (2707 kPa). The addition of the wheel loads led to a 27% increase in tensile stress. Inductive pavements can expect to experience similar levels of maximum tensile stress resulting from traffic and thermal loading conditions.

4.2 Fatigue Analysis

Most highways, and other major pavement structures, are designed to have a 20-year service life. Roadways will typically experience thousands of loading events throughout this lifespan. Subsequently, fatigue failures are one of the major concerns when designing a roadway for durability. Fatigue considerations vary depending on the type of material used. Asphalt pavements have different fatigue mechanisms than concrete and composite pavements. Concrete was initially chosen as the IPT system's embedment material, this analysis will focus on what happens to concrete during a fatigue failure. Although fatigue failures in concrete cannot be accurately predicted, the available information regarding concrete fatigue will be reviewed to better understand the failure/cracking mechanisms.

As stated in the previous section, heavy truck wheel loads and thermal loadings are the leading causes of roadway failures. Cracking often develops because of the repeated

tensile forces that are induced from these loading events. Once a crack develops, the opening allows for water and other contaminants to infiltrate the pavement structure and accelerate the pavement degradation. It is possible that the discontinuities created by the IPT system will increase the pavement's likelihood of developing cracks early in its service lifetime. Researchers wish to better understand the quantity and magnitude of tensile loading events an embedded IPT pavement can withstand without developing cracks.

Most material fatigue analysis, such as steel fatigue, is approximated by a plot of stress vs number of cycles to failure or S-N curve. Empirical data is typically used to generate an S-N curve, the curve can then be used to approximate the number of cycles to failure given a certain stress. Although the principles of a S-N curve can be applied to concrete fatigue, the properties of concrete make generating an accurate S-N curve difficult.

Concrete is considered a heterogeneous material because it is made up of cement, various aggregate materials and sizes, voids and other flaws. (Lee & Barr, 2002) states that concrete fatigue failure can be divided into 3 stages. The first stage is called flaw initiation. In this stage cracks originate in the weak regions within the concrete matrix. The second stage is characterized as microcracking, and involves the growth of the flaws that developed in the first stage. The third and final stage happens when a sufficient number of unstable microcracks have developed and a continuous crack forms, eventually leading to complete failure. Interestingly, the number of cycles required to reach failure will influence the types of cracks that form.

Lee & Barr (2002) claim that for a low cycle fatigue the dominant mechanism is

mortar cracks, which are characterized by microcracks that form between aggregate within the concrete matrix. These cracks form cracking networks and lead to a relatively quick failure. This type of fatigue failure is common for concrete structures subjected to earthquakes or other high impact forces.

Lee & Barr (2002) state that high cycle fatigue produces bond cracks around the aggregate. This type of cracking eventually leads to failure, but it is usually a slower and more gradual process. Table 4-1 from (Lee & Barr, 2002) below shows the number of cycles to failure for low, high and super-high cycle fatigue, as well as the types of structures that may experience this type fatigue loading. It can be surmised from Table 4-1 that roadway structures will be classified in the High-cycle fatigue range. Specifically, researchers can expect highways, and other roadway pavements, to experience between 100,000 and 1,000,000 cycles during their service lifetime. High cycle fatigue is classified as between 1,000 and 1,000,000 loading events.

The target fatigue stress level can then be determined using the number of cycles the roadway is expected to experience. (ACI 1997) states “*The fatigue strength of concrete is defined as a fraction of the static strength that it can support repeatedly for a given number of cycles*”. Using empirical data, (ACI 1997) developed a S-N plot showing the

Table 4-1 Classes of fatigue load (Lee & Barr, 2002)

<u>Low-Cycle Fatigue</u>			<u>High-cycle Fatigue</u>				<u>Super-high-cycle fatigue</u>		
1	10 ¹	10 ³	10 ³	10 ⁴	10 ⁵	10 ⁶	10 ⁷	10 ⁸	10 ⁹
Structures subjected to earthquakes			Airport pavements		Highway pavements		Mass rapid transit		Sea structures

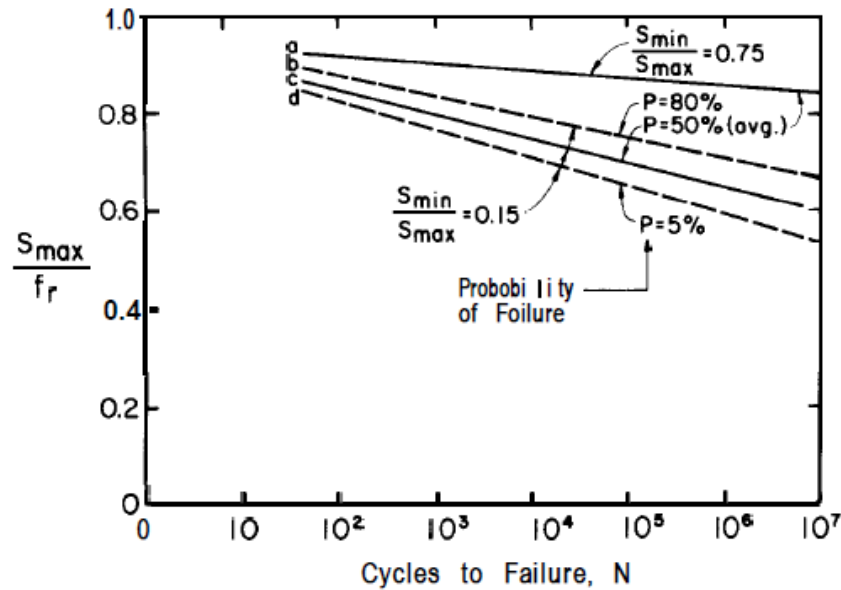


Figure 4-3 Concrete S-N plot

expected cycles to failure given the ratio of the induced tensile stress versus the rupture tensile stress (see Figure 4-3 above). Using data from the plot above it is estimated that concrete will have an 80% probability of cracking in tension at 100,000 cycles when the max tensile stress is approximately 70% of the modulus of rupture.

The Portland Cement Association (PCA) recommends another method. The following equation from (Dere, et al. 2006) can be used to calculate the maximum allowable number of repetitions concrete can withstand given a certain loading.

$$\text{For } SR = 0.55: \log_{10} N = 11.737 - 12.077SR \quad \text{Equation 4-1a}$$

$$\text{For } 0.45 < SR < 0.55: N = \left(\frac{4.2577}{SR - 0.4325} \right)^{3.268} \quad \text{Equation 4-1b}$$

$$\text{For } SR = 0.45: N = \text{unlimited} \quad \text{Equation 4-1c}$$

Where:

SR = The stress ratio, or the flexural stress divided by the 28-day modulus of rupture

N = The allowable number of load repetitions

Using 100,000 as the target number of cycles to failure, equation 4-1a can be rearranged to solve for the stress ratio. The equation gives a ratio value of 0.56. Note that this ratio is much more conservative than the ratio approximated from the S-N plot from (ACI 1997) on the previous page. The least conservative ratio of .70 from Figure 4-3 will be used to calculate the expected cracking stress at 100,000 cycles.

4.3 Fatigue Testing Set-up and Equipment

The fatigue testing will take place at USU's Systems, Materials, and Structural Health (SMASH) laboratory. This facility is specifically designed to destructively test a wide variety of structures and materials. Some of the major equipment that will be used for testing includes a MTS 110-kip servo hydraulic actuator along with its controlling software and a load frame designed to withstand 1200 kips of shear. Figure 4-4 on the next page shows the load frame to be used for the fatigue testing.

As discussed in (Xu et al. 2011), a common way to simulate roadway stresses is to use a four-point bending test. (Xu et al. 2011) states that "*periodic cracks always occur in the bending zone of the pavement*". A four-point bending test will allow for controlled, repeatable loadings to achieve the expected tensile stresses a roadway will experience throughout its lifetime. Figure 4-5 shows the four-point loading set-up that will be used to test the samples in fatigue. Figure 4-6 show the moment induced on the pad resulting from the four point bending test.



Figure 4-4 SMASH laboratory load frame



Figure 4-5 Four-point bending test set up

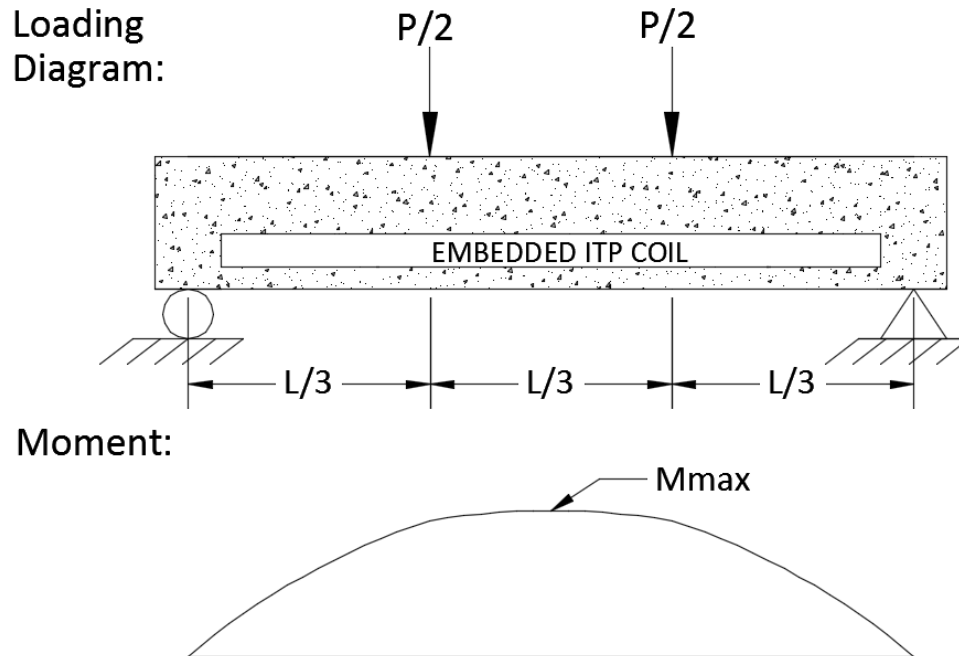


Figure 4-6 Four-point bending test loading diagram

A hydraulic actuator from MTS testing, will be used to apply the required force for the fatigue loading. The actuator is capable of applying loads up to 110 kips at a frequency of 200 cycles per minute. The loading force and frequency are adjusted through the MTS computer software. The hydraulic actuator has an integrated load cell that can be monitored controlled with the MTS software. Data acquisition for the testing will include the applied load on the concrete pad as well as the displacement during the fatigue testing process.

4.4 Determining f_r

To determine the cracking stress given the number of loading cycles, the modulus of rupture for the concrete used in the samples had to be obtained. Because the same concrete mix design was used for each sample, the modulus of rupture is expected to be

consistent for each sample. A split tension test was set up to determine the approximate rupture stress of the concrete. The first series of split tension tests used concrete cylinder samples taken during the last concrete pour (shown in Table 4-2). The cylinder's dimension for the samples were a diameter of 4 inches, and a length of 8 inches. Along with the concrete cylinder samples, two core samples were taken from one the concrete pads from a different pour approximately 90 days after the concrete pour.

The dimensions of the core samples were a diameter of 3 inches and a length of 7.5 inches. The results of the core sample split tension test are shown in Table 4-3 on shown below. Note that because of the core drill size available, the dimensions of the core samples were different than the concrete cylinder samples. Equation 4-2 below is used to relate the applied load for the split tension test to the split tension tensile strength. This equation will provide the approximate tensile strength of the concrete.

Table 4-2 Concrete cylinder split-tension test results

Test #	Test #1	Test #2	Test #3	Average:
Total applied load (lbs.):	22,320 lbs.	28,137 lbs.	25,713 lbs.	25,390 lbs.

Table 4-3 Core sample split-tension test results

Test #	Test #1	Test #2	Average:
Total applied load:	21,968 lbs.	17,648 lbs.	19,808 lbs.

$$f_{sc} = \frac{2P}{\pi LD}$$

Equation 4-2

Where:

f_{sc} = Split-tension tensile strength (psi)

P = Total applied load (lbs.)

L = Sample length (inches)

D = Sample diameter (inches)

The average applied load and sample dimensions from the concrete cylinder split-tension test were used in equation 4-2, this gave a f_{sc} equal to 505 psi. The average applied load and sample dimensions from the core sample split-tension gave a f_{sc} equal to 515 psi.

Another method to determine the rupture strength is to relate the rupture strength to the compressive strength. The American Concrete Institute (ACI) defines f_r (modulus of rupture) as a function of the compressive strength f'_c with equation 4-3 shown below.

$$f_r = 7.5\lambda\sqrt{f'_c} \quad \text{Equation 4-3}$$

Where:

f_r = Modulus of rupture (psi)

f'_c = 28-day compressive strength (psi)

λ = Design safety factor, will be considered 1.0 in this case

Three cylinder samples from the first concrete pour were tested in compression.

The compressive strengths from this testing are recorded in table 4-4 below.

Table 4-4 28-day break tests

Test #	Test #1	Test #2	Test #3	Average:
Strength (psi)	7126 psi	7412 psi	7050 psi	7196 psi

Using this average 28-day compressive strength in equation 4-3 gives a f_r equal to 636 psi. This value is higher than both split-tension tensile strengths. The most conservative tensile strength comes from the average of the concrete cylinder split-tension tests, which was 505 psi. This will be the f_r value used in the S-N plot (see Figure 4-3) to calculate the cycles to failure. Figure 4-7 and Figure 4-8 below show the split-tension test set-up and procedure.



Figure 4-7 Split tension test set up



Figure 4-8 Split tension test

4.5 Determining S_{max}

The four-point bending test will produce the maximum tensile stress in the bottom of the pad. This tensile stress is meant to represent the tensile stress expected in the roadway surface. The concrete sample will be inverted with the embedded IPT coil closest to the bottom surface to simulate actual roadway conditions. Equations 4-3 and 4-4 on the next page show how the typical max moment and tensile stress will be calculated for the fatigue testing.

Each of the samples that will be tested contain discontinuities close to the tensile surface. The tensile stress is likely to increase because of the presence of the IPT system. While it is difficult to know how much these discontinuities will affect the tensile stress at the surface of the concrete, there will be two cases considered to calculate an approximate S_{max} . These two assumptions will change the cross-sectional properties of the concrete sample (location of the centroid, and the moment of inertia). The first assumption is that the concrete sample is completely homogenous with no discontinuities (see Figure 4-9 below). The dimensions from the small concrete samples are used for the cross-section property calculations.

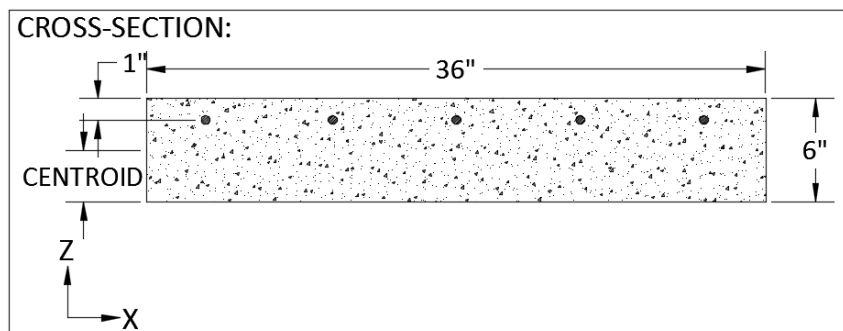


Figure 4-9 No discontinuity assumption cross-section

The cross-sectional properties are obtained from equations used appendix A. The centroid in the Z direction of this cross-section is 3.037 inches, and the moment of inertia about the cross-section's centroid about the X axis is 664 inches⁴. This assumption will be considered the least conservative when calculating S_{max} in the four-point bending test.

The second case assumes that a full de-bonded effect is created between the concrete and the components of the IPT system (see Figure 5-10 above). This can be

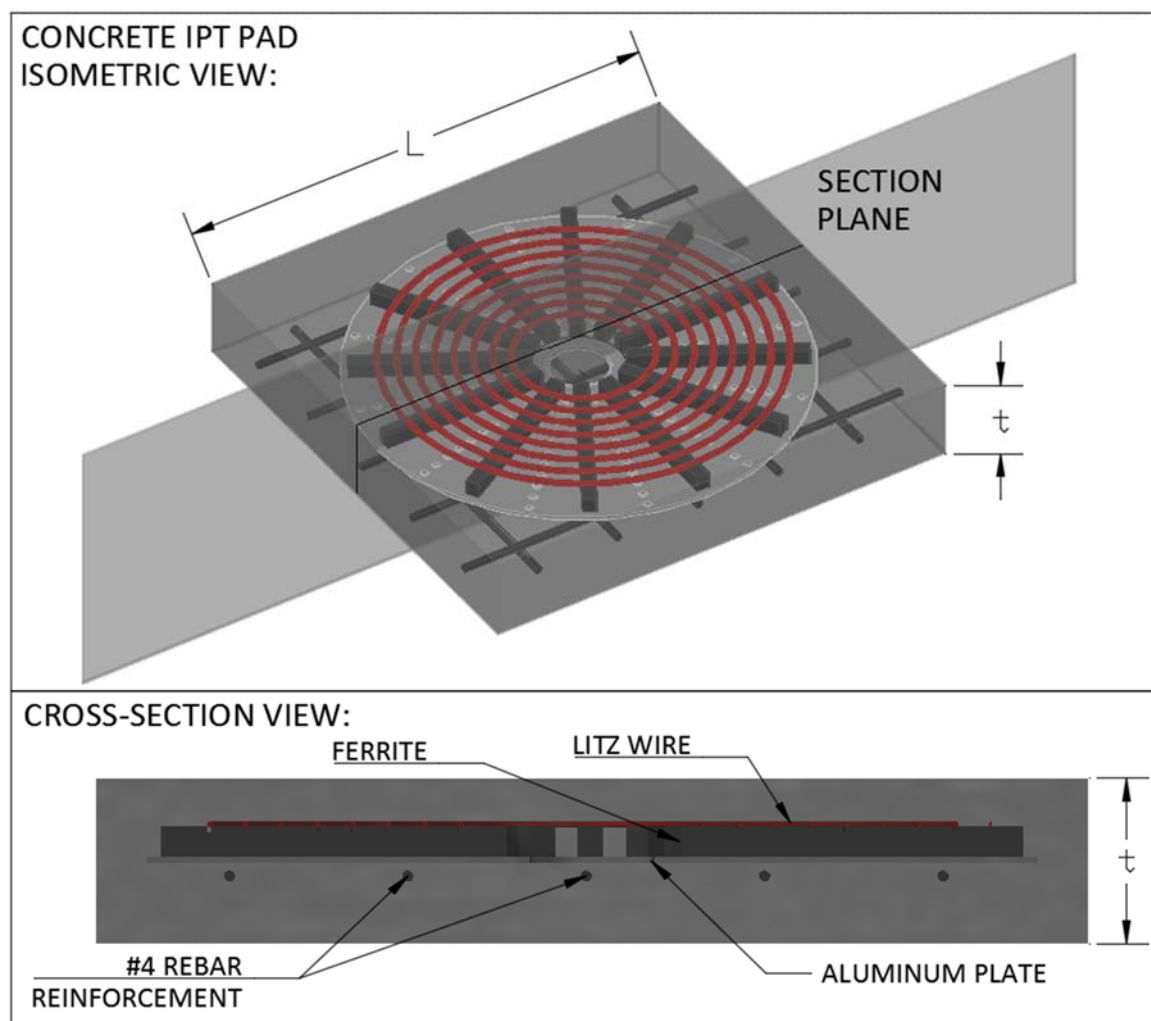


Figure 4-10 Concrete IPT pad Isometric and cross-section views

idealized by representing the de-bonded region as a void in the concrete cross-section. It is expected that the presence of the void will reduce the concrete pad's moment resistance. Figure 4-11 shows the second case's cross section and void size assumptions.

The cross-sectional properties are again obtained from appendix A. The centroid in the Z direction of this cross-section is 3.613 inches, and the moment of inertia about the cross-section's centroid about the X axis is 449.2 inches⁴. This assumption will be considered the most conservative when calculating S_{max} in the four-point bending test.

As discussed previously, Figure 4-6 shows the moment distribution for a four-point bending test. Equations 4-4 and 4-5 below are used to calculate the maximum moment and maximum stress for the two cases mentioned. These equations are re-arranged in equation 4-6 to find the applied load required to achieve the desired stress.

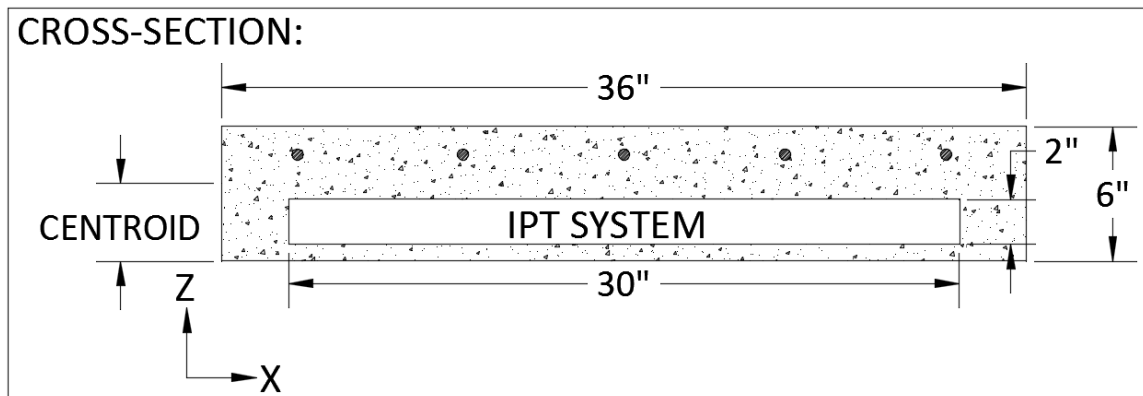


Figure 0-11 De-bonded discontinuity assumption

$$M_{max} = \frac{SW * L^2}{8} + \frac{P * L}{6} \quad \text{Equation 4-4}$$

$$S_{max} = \frac{M_{max} * Z_{bar}}{I_z} \quad \text{Equation 4-5}$$

$$P = \frac{3 * (8 * I_x * S_{max} - L^2 * SW * Z_{bar})}{4 * L * Z_{bar}} \quad \text{Equation 4-6}$$

Where:

M_{max} = Maximum moment

SW = Self-weight of the concrete sample

L = Sample Length

P = Applied load

S_{max} = Maximum stress in the bottom fiber of the sample

Z_{bar} = Distance from the centroid to the most extreme bottom fiber

I_z = Sample moment of inertia about its centroid

The cross-sectional area of the sample is 261 inches². The weight of reinforced concrete per cubic foot is taken as 150 lbs./ft³. Multiplying these factors give a self-weight of the concrete as 18.75 lbs./in. (225 lbs./ft.). Using the S_{max} to f_r ratio of .70, obtained from the S-N plot in Figure 4-3, the S_{max} to be used in equation 4-3 will be 354 psi. The samples are 36 inches long, but sample will be supported 1.0 inch from the edge. This will make L in the applied load calculation equal to 34 inches.

Equation 4-3 is solved for the applied load (P) using the cross-sectional properties obtained from the first assumption. The centroid (Z_{bar}) will be 3 inches, and the moment of Inertia I_z will be 648 inches⁴. The required applied load to produce 354 psi assuming a

completely homogenous concrete slab (no discontinuities) is 13,020 lbs. The Z_{bar} in the second assumption (fully de-bonded discontinuities) is 3.48 inches and the I_z is 498.2 inches⁴. Using these properties in the same equation requires an applied load of 8,500 lbs. to produce 354 psi in the bottom of the slab. Table 4-5 below compares the two assumptions.

It is likely that the actual load to achieve 354 psi in the bottom fiber is somewhere between these two assumptions. The cyclic loading will begin with the lowest applied load in order to maximize the number of cycles to failure in the first test. After the results from the first test will be analyzed before more tests are completed. The next tests will be adjusted to achieve the desired number of cycles to failure.

Researchers not only hope to understand how the discontinuities of the IPT system will affect the concrete pad's fatigue performance, but also study the IPT systems electrical performance during a fatigue failure. Microcracking will develop as the concrete structure approaches its fatigue limit. By maximizing the number of cycles to failure, the amount of microcracking that develops should also be maximized. Researchers hope to understand

Table 4-5 Summary of assumptions

Assumption:	No discontinuities, no de-bonding	Discontinuities are fully de-bonded
Centroid (Z_{bar}):	3.037 inches	3.52 inches
Moment of Inertia (I_x):	664 inches ⁴	507.4 inches ⁴
Required P to reach 354 psi in the bottom fiber of the concrete (lbs.)	13,200 lbs.	8,500 lbs.

what effects these microcracks will have on the electrical properties of the IPT system. The electrical properties of each pad will be recorded during the testing to see at what point during the fatigue process the electrical properties change.

The loading frequency will follow a simple sine wave that will be force controlled, and will be applied at a rate of 70 cycles per minute. This rate comes from (ACI 1997) which states: “*Several investigations indicate that variations of the frequency of loading between 70 and 900 cycles per minute have little effect on fatigue strength provided the maximum stress level is less than about 75 percent of the static strength. For higher stress levels, a significant influence of rate of loading has been observed*”. The calculated tensile stress is assumed to be approximately 70 percent of the concrete’s rupture stress. Because this tensile stress level is less than 75% of modulus of rupture, other influences from the rate of loading will not be considered.

CHAPTER 5

TESTING RESULTS

Three different pads were tested using the methods described in the previous chapter. This chapter summarizes the results from fatigue testing these samples. The samples used for the fatigue testing were obtained from the different embedment methods described in chapter 3. The concrete pad dimensions, as well as the embedded IPT system properties varied with each pad.

The goal of this testing is to first understand how the presence of the IPT system effects the structural performance of the pavement structure (concrete slab); and second, understand what happens to the electrical properties of the IPT system as the pavement structure is fatigued and approaches failure. The data that will be recorded includes the number of loading cycles, the deflection during each loading cycle and number of cycles at which the concrete first starts to show cracking. The initial electrical properties as well as the change in these properties will be recorded throughout the entire testing process. The concrete sample is expected to reach a structural failure when it can no longer support any load.

5.1 Fatigue Testing First Pad

The first pad tested in fatigue was the third sample from chapter 3. This pad is 36 inches wide, 36 inches long, and 6 inches deep. The IPT system includes the coil of Litz wire, the ferrite, and a wood plate to hold the components in place. The wood plate is approximate size and shape that an aluminum shielding plate would be in other IPT

systems. Rebar reinforcement was used in this sample. The initial electrical properties are recorded to use as a reference as the pad is fatigued until failure. These properties will be continually monitored throughout the fatigue process as the pad cracks, and as the size of these cracks grow (shown in table 5-1).

The four-point bending method was chosen because it creates a constant tensile stress throughout the middle third of the beam (see *Figure 4-6*). To crack the concrete pad at 100,000 cycles, the ratio of applied stress to rupture stress is expected to be .70 obtained from the S-N plot from (ACI 1997). As previously stated in section 4.4, the expected tensile stress to crack at 100,000 cycles is 354 psi. The calculated load to achieve this tensile stress, based on the second assumption, is 8,500 lbs. A trial run with the applied load of 7,500 lbs., 1,000 lbs. lower than the calculated load, will be initially run to assess the sample's response. After the trial run is completed, the full calculated load will be applied to the pad. *Figure 5-1* shows the set up for the first sample before the testing begins.



Figure 5-1 First fatigue test set-up

After the pad was loaded approximately 100 times major cracking occurred. The major cracking was observed by the appearance of a large crack through the middle of the pad and an increase in deflection. The cycle data on the hysteresis plot above reflects the pre-cracking cycles, the crack initiation, and the post-cracking cycles. After the first major sign of cracking, the pad was loaded approximately 20,000 more times with the same load. After the pad developed its first crack then the deflection of the pad reached a steady state where the deflection no longer increased with each load (see Figure 5-2).

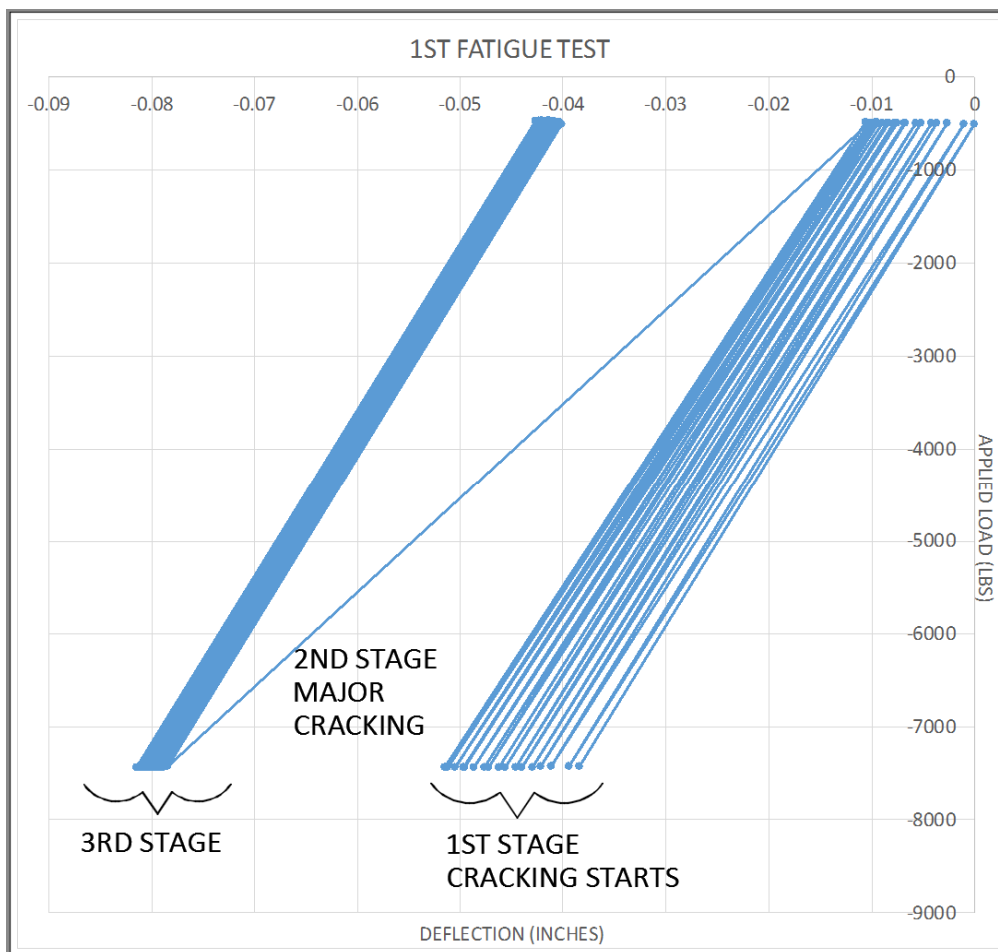


Figure 5-2 Hysteresis of first fatigue test

After the pad reached a steady state where relative deflection no longer increased the load was increased periodically in 2,000 lbs. increments. After the first cracks appeared it was important for researchers to learn how the electrical properties were affected by the continued cracking of the pad. Table 5-1 shows the change in electrical properties during the fatigue process. (Figure 5-3 through 5-9 on the following pages show the pre-cracked pad and the crack initiation and progression).



Figure 5-3 Pre-cracked pad



Figure 5-4 First Stage (100 cycles)



Figure 5-5 Second Stage (15,000 cycles)



Figure 5-6 Load was increased to 9,000 lbs. (approximately 20,000 cycles)



Figure 5-7 Cracks 1/2 inch (approximately 25,000 cycles)



Figure 5-8(approximately 27,000 cycles)



Figure 5-9 First pad post failure

Table 5-1 First sample: change in electrical properties with crack size

	Initial Inductance/ Resistance	Crack Size (inches)					
		0.0625"	0.125"	0.25"	0.5"	0.625"	0.75"
1 st Test	115 μ H 1.5 Ω	115.2 μ H 1.3 Ω	111.7 μ H 1.05 Ω	111 μ H 1.7 Ω	Wire Sheared	N.A.	N.A.

As stated in the previous chapter, the goal of the fatigue testing was to have the concrete fail in tension at 100,000 cycles. Although the load was reduced because the effect of the IPT system on the tensile stress was unknown, the sample failed well below the target number of cycles. After the concrete cracked it is believed that most of the tensile stress was being carried by the Litz wire, much like rebar reinforcement works in a reinforced concrete beam. The deflection remained constant during the last 20,000 cycles with the load at 7500 lbs. The load was then increased to effectively measure the electrical properties as the cracks grew wider.

The electrical properties of the pad showed relatively little change as the pad initially developed cracks. The table above shows the change in inductance and resistance as the width of the cracks increased. As shown in the table, the electrical properties suddenly changed when the crack widths reached $\frac{1}{2}$ of an inch wide. It is believed that the Litz wire sheared at this point resulting in a sudden drop in inductance. At the time of failure, the applied load was approximately 11,500 lbs.

5.2 Fatigue Testing Second Pad

The second pad tested in fatigue had the same dimensions as the first pad: 36 inches wide, 36 inches long, and 6 inches deep. The electrical components of this sample included

an aluminum shielding plate, ferrite bars, and the coil of Litz wire. The applied load during each cycle was reduced from the first test by 1750 lbs. By reducing the applied load by this amount, the maximum moment felt in the center of the pad was reduced by approximately 20 percent.

The pad showed relatively little change in deflection during the first 10,000 loading cycles as reflected in the 1st stage in Figure 5-10. Around 10,000 loading cycles the pad

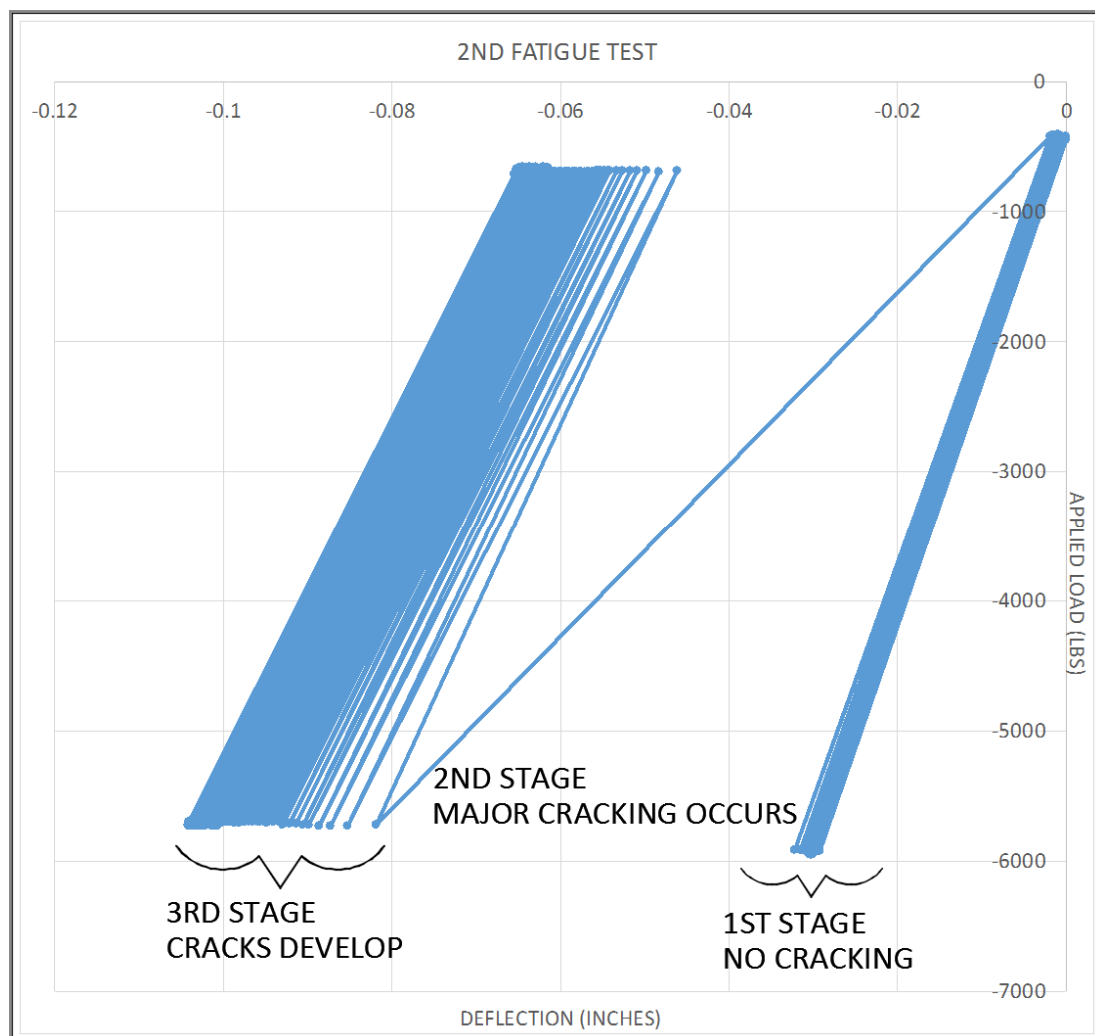


Figure 5-10 Hysteresis of second fatigue test

developed a large crack in the center of the sample and a large increase in the total deflection. After this sudden development of cracking the sample continued to experience a gradual deflection increase throughout the next 30,000 loading cycles as the cracks grew wider. After 30,000 cycles the sample seemed to reach a steady state where the deflection no longer increased. At this point the load was again increased in 2,000 lbs. increments to continue to measure the electrical properties as the concrete continued to crack. Figures 5-11 through 5-17 show the cracking initiation and propagation.



Figure 5-11 Pre-cracked pad



Figure 5-12 Second Stage (approximately 10,000 cycles)

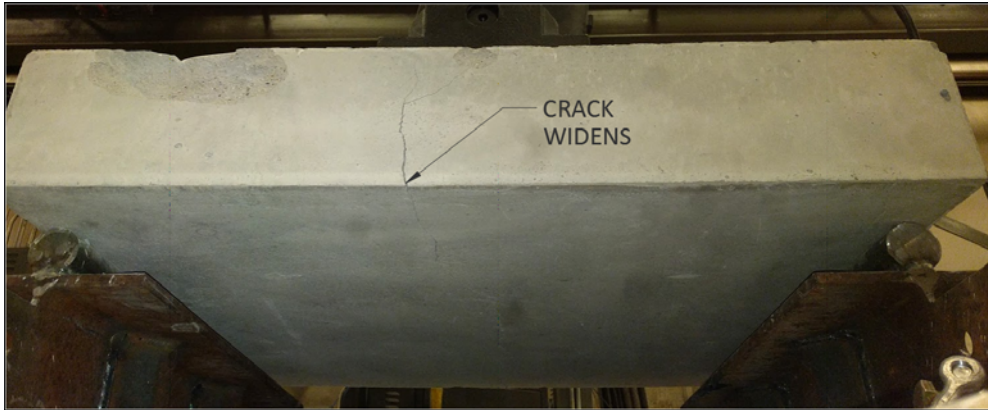


Figure 5-13 Third Stage (approximately 30,000 cycles)



Figure 5-14 Crack 1/4 inch wide, load increased (32,000 cycles)



Figure 5-15 Crack 3/8 inch wide, (35,000 cycles)



Figure 5-16 Crack $\frac{3}{4}$ inch wide, (36,000 cycles)



Figure 5-17 Failure (approximately 40,000 cycles)

The number of cycles required to experience major cracking was 10,000 cycles, and the cracks continued to develop under the same load for another 20,000 cycles. Although the target of 100,000 loading cycles was not achieved, the cracking mechanism, explained in (Maekawa et al. 2006) for high cycle fatigue, should be the same. The crack development in second sample was similar to the first sample, a crack formed down the center of the pad then after the load was increased a larger crack formed around the

circumference of the aluminum plate that eventually led to failure. Figure 5-18 shows these two locations of cracking.

Table 5-2 Second pad change in electrical properties with crack size

	Initial Inductance/ Resistance	Crack Size (inches)					
		0.0625"	0.25"	0.5"	0.75"	1"	2"
2 nd Test	123.33 μ H .1118 Ω	123.07 μ H .121 Ω	123.07 μ H .126 Ω	122 μ H .207 Ω	122 μ H .216 Ω	114 μ H .213 Ω	Wire Sheared

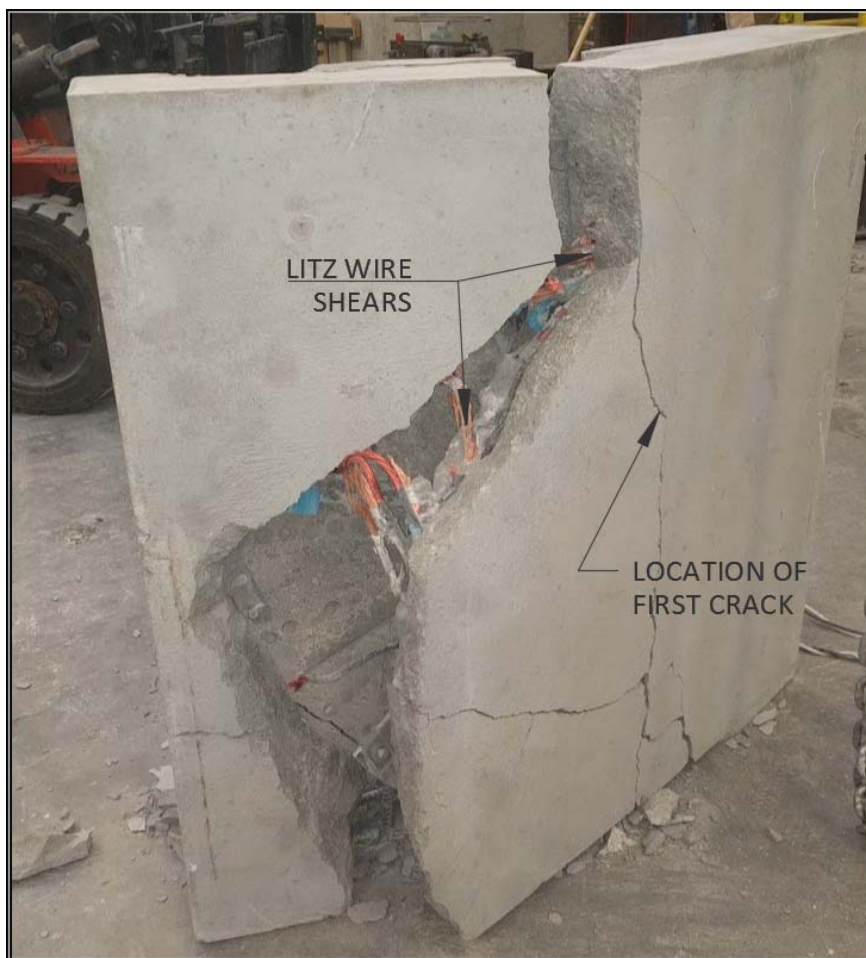


Figure 5-18 Second pad post failure

The changes in the electrical properties were also similar to the first sample. There were relatively no significant electrical changes until the cracks grew to around 2 inches. After the crack widths reached 2 inches the electrical properties experienced a sudden change probably due to the shearing of the Litz wire. Figure 5-18 shows the second sample after the fatigue failure.

5.3 Fatigue Testing Third Pad

The third pad tested in fatigue was the first full-sized pad mentioned in chapter 3. The pad's components included a coil of Litz wire, an aluminum plate, ferrite bars, and rebar reinforcement. The dimensions of this pad are 42 inches wide, 42 inches long and 10 inches tall. The four-point bend test was modified from the previous two tests to load the new sample at every 4th point along its length, see Figure 5-19 below. The initial electrical properties were recorded to measure the change in these properties as the concrete was fatigued (see Table 3-1 for pre-embedment electrical properties).



Figure 5-19 Third fatigue test set-up

The calculated tensile stress in the bottom fiber of the pad was again reduced from the previous test in order to reach 100,000 loading cycles before the concrete failed in tension. This sample had several existing cracks that developed after it was taken to the EVR. It is expected that the presence of these cracks further reduced the tensile strength of the concrete.

The applied load on this sample was 14750 lbs. The load was applied 100,000 times. Unlike the previous two tests, this sample did not experience a major cracking event that caused a sudden increase in deflection. Also unlike the previous two tests, the deflection consistently increased throughout the test (See Figure 5-20 below). Figure 5-21 through 5-27 show the cracking development throughout the fatigue test.

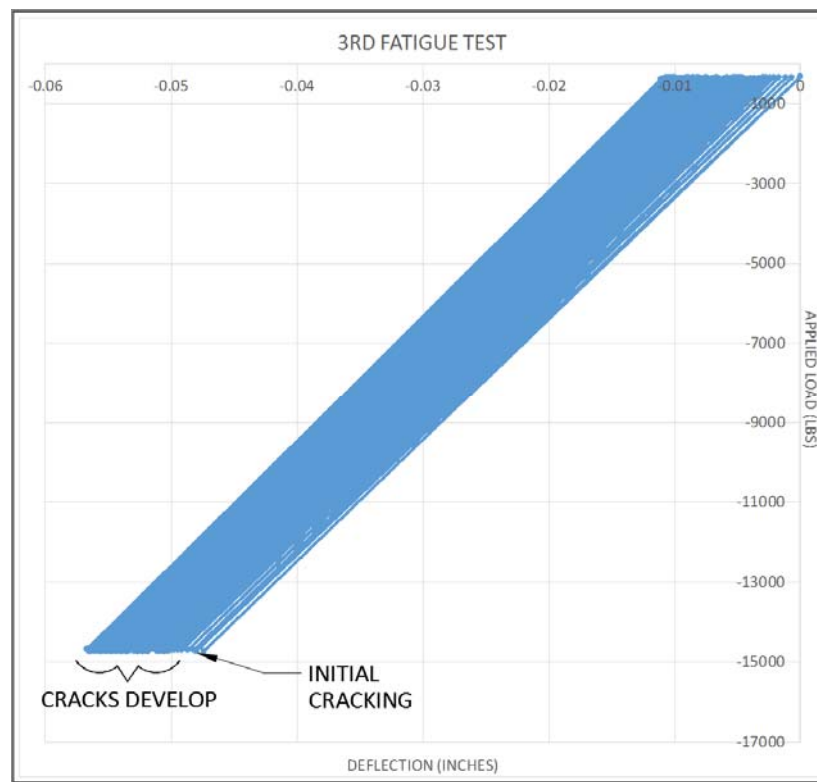


Figure 5-20 Hysteresis of third fatigue test



Figure 5-21 Pre-cracked pad



Figure 5-22 Cracking develops



Figure 5-23 Crack 1/8 inch wide



Figure 5-24 Crack 1/4 inch wide



Figure 5-25 Crack 1/2 inch wide



Figure 5-26 Pad after failure



Figure 5-27 Third pad post failure

After 100,000 cycles, the applied load on the pad was incrementally increased by 2,000 lbs. every 2,500 cycles so that the electrical property changes of the system could be assessed. Table 5-3 shows that there was almost no change in the electrical properties of the system early in the fatigue process, and minimal changes up to the complete failure of the pad. The value of inductance after failure is 3% lower than the initial value, and the

Table 5-3 Third pad change in electrical properties with crack size

	Initial Inductance/ Resistance	Crack Size (inches)					
		0.0625"	0.25"	0.5"	0.75"	1"	2"
3 rd Test	179.5 μ H 2.66 Ω	176 μ H 2.91 Ω	178.5 μ H 3.8 Ω	175.8 μ H 3.11 Ω	179 μ H 3.61 Ω	175 μ H 3.7 Ω	174 μ H 3.6 Ω

value of resistance after failure is 26% higher than the initial value. *Figure 5-27* shows that unlike the previous two tests, the cracking of the concrete doesn't appear to have sheared the Litz wire.

5.4 Other Cracking Results

Another pad was tested with the four-point bending procedure described in the previous three tests shown in *Figure 5-28* and *5-29*. This sample contained the Litz wire coils, ferrite, and wire holders as found in previous samples. The pad did not have any rebar reinforcement or aluminum shielding plate. The goal of this test was to determine how the absence of the aluminum plate effected the strength of the pad.

The pad was initially loaded with the intent of conducting a cyclic loading test. The applied load was set to cycle at 12800 lbs. (This was the load determined from the first assumption). When the applied load on the pad reached 1150 lbs. the sample cracked. Although this cracking was not the result of a fatigue load, its strength will be considered when comparing the other fatigue loading results. It should be noted that the wire holders for this sample represented a large discontinuity in the sample's cross-section. It should also be noted that as with the previous tests described, the cracking did not change the electrical properties of the pad.



Figure 5-28 Other Sample tested with four-point bending test



Figure 5-29 Other sample after failure

5.5 Summary of Results

In each of the fatigue tests the embedded IPT systems showed relatively small changes in the electrical properties as the concrete developed its initial cracking. In the first two tests, as the concrete approached failure, the concrete cracking sheared the Litz wire

and caused an immediate loss in the electrical properties of the IPT system. In the final test the concrete cracks never sheared the Litz wire, and the concrete experienced relatively small electrical changes even after the complete failure of the concrete pad.

Each of the samples followed relatively the same failure process. First the samples developed an initial crack through the center of the pad at the location of the largest moment. Then the pads reached a steady state where there was relatively no increase in deflection. After they reached this steady state under the initial load, the load was increased and the concrete failed in a circular shape around the Litz wire coil. It is believed that the Litz wire acted much the same way as rebar reinforcement in a concrete beam after the initial cracking occurred.

Chapter 4 describes the two assumptions used to calculate the possible tensile stress in the bottom fiber of the concrete. These assumptions were considered to be the most and least conservative values that the tensile stress would be given the concrete sample's cross-sectional properties. It was believed that the actual value of tensile stress would be somewhere between these assumptions. In each test the concrete cracked below the most conservative assumption. Table 5-4 below shows the tensile stress at cracking for each pad. For comparison purposes, the cross-sectional properties are assumed to be the same as those made in assumption 1 (there are no discontinuities represented in the calculations for the moment of inertia or the centroid). This will allow for a direct comparison of the fatigue strength between the samples.

Figure 5-30 shows the calculated static strength of a concrete sample without the embedded IPT system. The probability of failure lines (shown in black) for the fatigue of

a pad without the embedded system come from (ACI 1997). The blue point and line represent the static strength of the IPT system without the embedded shielding plate. The lowest red points and line represent the fatigue failure points of the IPT system with the embedded shielding plates.

Table 5-4 Tensile strength at cracking for each pad

Test #:	Test #1	Test #2	Test #3	Static Test
Tensile stress at cracking:	209.3 psi	163.4 psi	144.3 psi	348.3 psi
Ratio of S_{max} to f_r	0.41	0.322	0.28	.69
Number of cycles to initial cracking:	91 cycles	10,053 cycles	gradual cracking	1

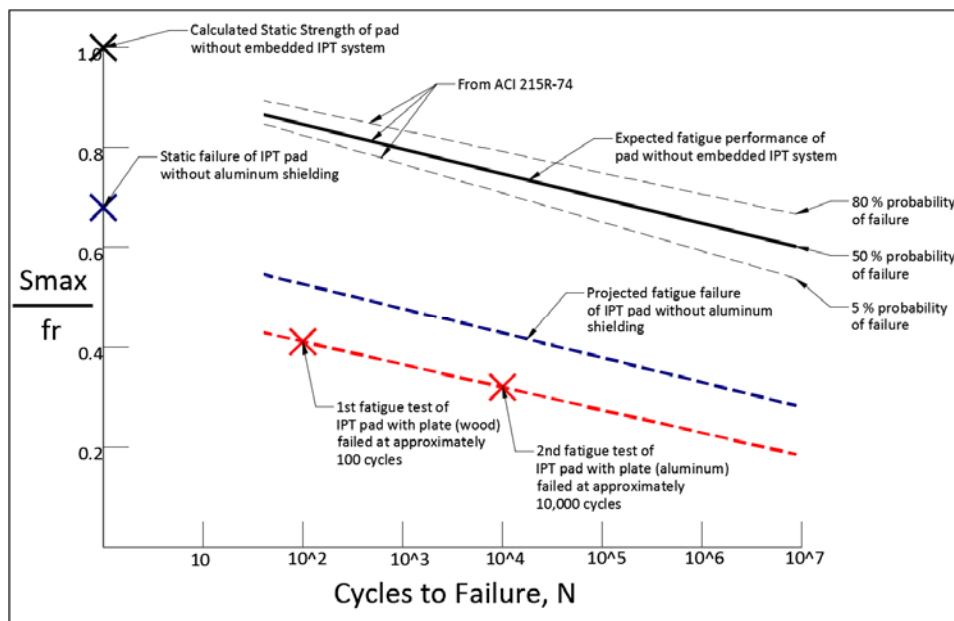


Figure 5-30 S-N testing results

CHAPTER 6

CONCLUSIONS

The integration of wireless power transfer systems into the infrastructure is divided into two sections. The first section of this thesis investigates various wireless power transfer integration techniques and testing methods. A direct embedment approach was initially taken, and concrete was chosen as an embedment material. The embedment process involved:

- Testing the interaction of individual components (such as Litz wire) with concrete.
- Directly embedding a full scale Inductive Power Transfer (IPT) system into a concrete pavement structure.
- Optimizing the electrical performance of several embedded IPT systems.

Findings:

- 1) It was determined that a wire thickness coating of 0.029 inches nearly eliminated the electrical performance losses from directly embedding the IPT coil in concrete.
- 2) The embedded IPT system with a shielding plate reduces the fatigue strength of the pavement structure by as much as 48 percent (see Figure 5-30). The aluminum shielding plate may be unnecessary and was omitted from the final design.
- 3) Without the aluminum shielding plate, the embedded system's fatigue strength was reduced by approximately 30 percent (see Figure 5-30).

- 4) It was found that the microcracking, that accompanies high cycle fatigue, has little to no effect on the electrical properties that were measured (inductance and resistance).

The optimization techniques and embedment methods were applied to a full scale embedded IPT system, which is currently in use at the test track at the Electric Vehicle and Roadway (EVR) facility. The performance of this embedded IPT system will be monitored as it is used in real world applications to dynamically charge electric vehicles. It is expected that the concrete embedment methods learned in this research will be used to embedded future IPT systems as the electrical and mechanical design of these systems evolve.

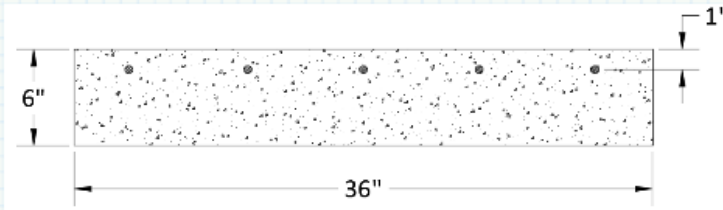
REFERENCES

- American Association of State Highway and Transportation Officials (AASHTO). (1993). *AASHTO Guide for Design of Pavement Structures*. Washington, D.C.: American Association of State Highway and Transportation Officials.
- American Concrete Institute (ACI). (1997). *ACI 215R-74 Considerations for Design of Concrete Structures Subjected to Fatigue Loading*. ACI Committee 215. American Concrete Institute.
- California Partners for Advanced Transit and Highways (PATH). (1994). *Roadway powered electric vehicle project track construction and testing program phase*.
- Chen, F., Taylor, N., & Kringos, N. (2015). Electrification of Roads: Opportunities and Challenges. *Applied Energy*, 109-119.
- Covic, G. A., & Boys, J. T. (2013). Inductive Power Transfer. *Proceedings of the IEEE*, 101(6), 1276-12889.
- Dere, Y., Asgari, A., Sotelino, E. D., & Archer, G. C. (2006). Failure Prediction of Skewed Jointed Plain Concrete Pavements Using 3D FE Analysis. *Engineering Failure Analysis*, 898-913.
- Lee, M., & Barr, B. (2002). An overview of the fatigue behaviour of plain and fibre reinforced concrete. *Cement and Concrete Composites*, 26, 299-305.
- Maekawa, K., Gebreyouhannes, E., Mishima, T., & An, X. (2006). Three-Dimensional Fatigue Simulation of RC Slabs Under Traveling Wheel-Type Loads. *Journal of Advanced Concrete Technology*, 445-457.
- Onar, O. C., Miller, J. M., & Campbell, S. L. (2013). A novel wireless power transfer for in-motion EV/PHEV charging. *Applied Power Electronics Conference and Exposition (APEC)*.
- Vliet, M. v., Gurp, C. v., Bondt, A. d., & Bijsterveld, W. v. (2005). Structural Viability of Shallow Depth Hollow Systems in Airfieldn Pavements. *1st European Airport Pavement Workshop*. Amsterdam.
- Xu, C., Anzhi, Y., Liao, M., & Chunan, T. (2011). Analysis of periodic cracks in surface layer of pavement structures. *Engineering Failure Analysis*, 18(1), 411-420.

APPENDICES

Appendix A: Calculating Moment of Inertia for Two Assumptions

Determine Centroid and Moment of Inertia of 1st assumption using Equivalent Area Method:



Concrete Properties:

$$f'_c := 7000$$

$$E_c := 57000 \cdot \sqrt{f'_c} = 4.769 \cdot 10^6$$

Steel Properties:

$$f_y := 60 \quad \text{ksi}$$

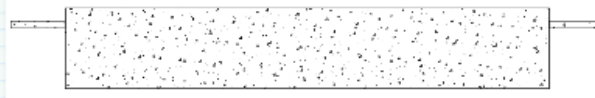
$$E_s := 29 \cdot 10^6 \quad \text{psi}$$

$$A_s := 4 \cdot .2 = 0.8 \quad \text{in}^2$$

$$n := \frac{E_s}{E_c} = 6.081$$

Equivalent area of concrete at reinforcement:

$$(n - 1) \cdot A_s = 4.065 \quad \text{in}^2$$



Find Centroid from the bottom of the cross section:

$$Z_{bar} := \frac{(6 \cdot 36) \cdot 3 + (4.065) \cdot 5}{(6 \cdot 36) + 4.065} = 3.037 \quad \text{inches}$$

Find Moment of Inertia:

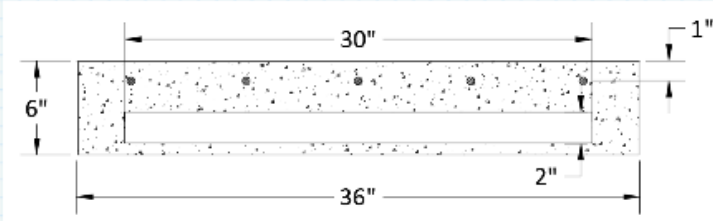
$$I_x := \frac{36 \cdot 6^3}{12} + (6 \cdot 36) \cdot (Z_{bar} - 3)^2 + 2 \cdot \left(\frac{4.065 \cdot 5^3}{12} + \left(\frac{4.065}{2} \right) \cdot (5 - Z_{bar})^2 \right) = 664.044 \quad \text{in}^4$$

Find applied moment for desired fatigue stress:

$$S_{max} := 354 \quad L := 34 \quad SW := 18.75$$

$$P := \frac{3 \cdot (8 \cdot I_x \cdot S_{max} - L^2 \cdot SW \cdot Z_{bar})}{4 \cdot L \cdot Z_{bar}} = 1.318 \cdot 10^4 \quad \text{lbs}$$

Determine Centroid and Moment of Inertia of 2nd assumption using Equivalent Area Method:



Concrete Properties:

$$f'_c := 7000$$

$$E_c := 57000 \cdot \sqrt{f'_c} = 4.769 \cdot 10^6$$

Steel Properties:

$$f_y := 60 \quad \text{ksi}$$

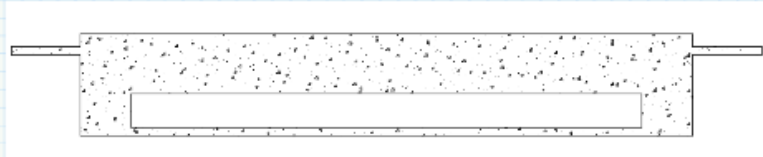
$$E_s := 29 \cdot 10^6 \quad \text{psi}$$

$$A_s := 4 \cdot .2 = 0.8 \quad \text{in}^2$$

$$n := \frac{E_s}{E_c} = 6.081$$

Equivalent area of concrete at reinforcement:

$$(n - 1) \cdot A_s = 4.065 \quad \text{in}^2$$



Find Centroid from the bottom of the cross section:

$$Z_{\text{bar}} := \frac{(3.25 \cdot 36) \cdot 4.375 + (4.065) \cdot 5 + (3 \cdot 2) \cdot 1.75 + (3 \cdot 2) \cdot 1.75 + (.75 \cdot 36) \cdot \left(\frac{.75}{2}\right)}{(3.5 \cdot 36) + 4.065 + 2 \cdot (3 \cdot 2) + (.5 \cdot 36)} = 3.519 \quad \text{inches}$$

Find Moment of Inertia:

$$I_x := \frac{36 \cdot 6^3}{12} + (6 \cdot 36) \cdot (Z_{\text{bar}} - 3)^2 + 2 \cdot \left(\frac{4.065 \cdot .5^3}{12} + \left(\frac{4.065}{2} \right) \cdot (5 - Z_{\text{bar}})^2 \right) - \left(\frac{30 \cdot 2^3}{12} + (2 \cdot 30) \cdot (Z_{\text{bar}} - 1.75)^2 \right) = 507.421 \quad \text{in}^4$$

Find applied moment for desired fatigue stress:

$$S_{\text{max}} := 354 \quad L := 34 \quad SW := 18.75$$

$$P := \frac{3 \cdot (8 \cdot I_x \cdot S_{\text{max}} - L^2 \cdot SW \cdot Z_{\text{bar}})}{4 \cdot L \cdot Z_{\text{bar}}} = 8.529 \cdot 10^3 \quad \text{lbs}$$